



An age-integrated geochemical and computational phase-equilibria study from the Wangtu Gneissic Complex, N-W Himalaya, and its paleogeographic implications in Columbia assembly

Hifzurrahman¹ · Pritam Nasipuri¹ · Keewook Yi² · Aryavart Anand³ · Sagar Misra¹ · Anil K. Champati⁴

Received: 10 August 2020 / Accepted: 21 January 2021 / Published online: 11 March 2021

© The Author(s), under exclusive licence to Springer-Verlag GmbH, AT part of Springer Nature 2021

Abstract

The Paleoproterozoic thermal evolution of the north-Indian continental margin is debatable as the Lesser Himalaya granites are interpreted either as a subduction-zone volcanic arc or rift-related magmatism during Columbia assembly or disintegration processes, respectively. Integrated mineralogical, geochemical investigations, temperature estimates from Ti solubility in biotite and zircon, and computational phase equilibria modeling from the Wangtu Gneissic complex (WGC), Himachal Himalaya reveal peraluminous nature for most of the WGC rocks that crystallize at ~650 °C and ~1.0–1.1 GPa. The U-Pb ages from magmatic zircons from the WGC exhibit two prominent age clusters at 1867 Ma and 2487 Ma. The U-Pb zircon data and modeled phase equilibria for metasedimentary rock reveal the generation of S-type peraluminous magma parental to the WGC, through melting of preexisting supracrustal rocks at ~1800 Ma, within ~850–900 °C and 1.1–1.2 GPa, similar to *P-T* conditions observed in modern-day subduction zone settings. The results obtained from this study reveal the north Indian continental margin was an active subduction zone during the Paleoproterozoic Columbia supercontinent assembly that extends across the Himalayas.

Keywords Columbia · Zircon · Geochronology · Subduction zone · U-Pb isotope · Lesser Himalaya

Introduction

The geological evolution of magmatic rocks and their high-precision U-Th-Pb geochronology provides a significant stimulus for reconstructions of ancient supercontinents, namely the Paleoproterozoic Columbia (Rogers and Santosh 2005; Rogers 2009; Zhao et al. 2011; Meert and Santosh 2017), the Mesoproterozoic Rodinia (Hoffman 1991; Dalziel et al. 2000)

and Neoproterozoic/Cambrian Gondwanaland (Collins and Pisarevsky 2005; Meert et al. 2013, 2017).

There is a general agreement that the Indian continent was an integral part of a Palaeo-Mesoproterozoic supercontinent, Columbia, that existed between 1900 and 1800. The Paleoproterozoic collisional orogenesis that framed the architecture of Columbia supercontinent for the Indian peninsula has been studied from the Satpura orogeny in Central India (Bhandari et al. 2011; Bhowmik et al. 2012; Bhowmik 2019), Aravalli-Delhi Orogeny in north-western India (Saha et al. 2008; Bhowmik et al. 2009; Kaur et al. 2013a), and the trans-north china orogen in China (Zhao and Zhai 2013). Also, the Paleo-Mesoproterozoic tectono-thermal activities related to Columbia assembly has been studied from the 1900–2000 Ma Capricorn orogen in western Australia (Van Kranendonk and Collins 1998), Nimrod Orogeny in Antarctica (Goodge et al. 2001; Goodge and Fanning 2016), the Kimbam Strangways orogeny in central Australia (Payne et al. 2009) and the Trans-Hudson Orogen in northern America (Hoffman 1988; St-Onge et al. 2007).

In the Indian peninsula, the high-grade rocks and granite magmatism in the Central Indian Suture (CIS) and its extension towards the east, and the Aravalli-Delhi Fold-Belt in north-western India, and the tectonic domains at the southern and

Editorial handling: Q. Li

✉ Pritam Nasipuri
pritam@iiserb.ac.in

¹ Department of Earth and Environmental Sciences, Indian Institute of Science Education and Research, Bhopal, Madhya Pradesh 462066, India

² Korea Basic Science Institute, Korea Basic Science Institute (KBSI), 162 Yeon Gu DanJi- Ochang, Cheongju-city, ChungBuk 28119, South Korea

³ Institute of Geological Sciences, University of Bern, Baltzerstrasse 1 + 3, CH-3012 Bern, Switzerland

⁴ Central Instrumentation Facility, New Petroleum Building, Indian School of Mines-Dhanbad, Dhanbad, Jharkhand 826004, India

eastern margin of Western Dharwar Craton (WDC) and Eastern Dharwar Craton (EDC) respectively, record evidence of Paleoproterozoic metamorphism that constitutes the framework of supercontinent Columbia in Indian perspective (Fig. 2, Chatterjee and Bhattacharji 2001; Kaur et al. 2007; Saha et al. 2008; Chatterjee and Ghose 2011; Kaur et al. 2011b, 2013a, 2015; Bhowmik et al. 2012; Sanyal and Sengupta 2012; Harley and Nandakumar 2016; Liu et al. 2017; Prakash et al. 2018; Bhowmik 2019). Also, researchers, as Upreti (1999); Miller et al. (2000); Richards et al. (2006); Chambers et al. (2009); Singh et al. (2009); Kohn et al. (2010); Phukon et al. (2018); Sen et al. (2019); and Singh (2020) document 2100–1800 Ma magmatic activity and granite emplacement from various stratigraphic levels from of Lesser Himalayan (LH) sequences. The geochemistry of LH granites and U-Pb zircon ages in the Himalaya are variably interpreted either as A-type granites that were emplaced during Columbia disintegration (Singh et al. 2009; Larson et al. 2019; Singh 2020) or mostly S-type granites that were emplaced at lower crustal levels during the final amalgamation of Columbia in a subduction zone settings (Chambers et al. 2008; Kohn et al. 2010; Kaur et al. 2013b; Sen et al. 2013; Phukon et al. 2018). Miller et al. (2000); Chambers et al. (2008); Kohn et al. (2010); Phukon et al. (2018); Pathak and Kumar (2019); Sen et al. (2019); and Mukherjee et al. (2019) provide geochemical and geochronological evidence supporting subduction zone tectonics and related magmatism in the LH sequences. Also, Kaur et al. (2009, 2011b) correlated the granites from the Aravalli craton with the LH granites and suggested LH granites were emplaced in a volcanic arc along North Indian Cratonic Block (NICB). However, Larson et al. (2019); Singh (2020) reported contradictory geochemical evidence supporting a rift-related passive margin.

The Aravalli craton and the Bundelkhand craton as part of NICB, the Dharwar, the Bastar, and the Singhbhum craton, as a part of South Indian Cratonic Block (SICB), amalgamated along the Central Indian Tectonic Zone (CITZ) to constitute the tectonic framework for traditional Columbia in Indian perspective. In the absence of reliable paleomagnetic data, the traditional Columbia reconstruction after Rogers and Santosh (2002) and Zhao et al. (2002) are principally based on chronologically correctable tectonic activities from the SICB as precise geochronological and metamorphic data from the NICB are meager. For example, the Mahanadi-Lambert rift in India-Antarctica landmass and rift basins in the western margins of present-day (North America Belt and Unita Trough) are temporarily correctable (Fig. 7.8 of Rogers and Santosh 2002). Accordingly, Rogers and Santosh (2002) placed eastern India adjacent to the western margin of North-America. Zhao et al. (2002) correlate 2100–1800 Ma geological data across major landmasses, supporting the traditional Columbia hypothesis.

Even after two decades of extensive research and its role in supercontinent assembly and destruction processes, the

tectonic evolution of the CITZ is debatable. The critical metamorphic ages from CITZ fall at 2500 Ma, 1600 Ma, and 1000 Ma. Stein et al. (2004) suggested NICB and SICB suturing occurred at 2500 Ma, followed by reworking at 1600 Ma and 1000 Ma. Basu Sarbadhikari and Bhowmik (2008); Bhandari et al. (2011); Mandal et al. (2013) contradict Stein et al. (2004) model and favor a 1600 Ma orogenesis involving SICB and NICB.

Hou et al. (2008) correlate the occurrences of 1800 Ma dyke swarms from North China Craton, SICB, and North America and suggest that these three cratons were united to form a landmass before its breakup at 1400–1300 Ma. In support of the growth of 1850 Ma Columbia supercontinent, Hou et al. (2008) suggest the occurrences of a subduction zone along the northern margin of NICB that was probably continuous with subduction zones along the south-eastern margin of North America, Greenland, Baltica to North-China craton - eastern Antarctica (Fig. 7 of Hou et al. 2008).

Meert and Santosh (2017) utilized the palaeomagnetic data to validate the traditional Columbia configuration. The paleomagnetic data imply Siberia, Laurentia, and Baltica constitute the coherent long-lived core (1900–1300 Ma) for the Columbia supercontinent (Evans and Mitchell 2011). However, in the absence of 1800–1600 Ma paleomagnetic data from the Indian subcontinent, the position of Indian in the Columbia framework remains problematic. Meert and Santosh (2017) placed India at a considerable distance from present-day Laurentian and close to Baltica based on ~1465 Ma Lakhna pole from SICB.

The absence of reliable geochronological and geochemical data from the northern extremity of the Indian shield leads to three possible scenarios: (i) India-Madagascar-Kalahari-Zimbabwe-Australia, and parts of Antarctica formed a single continental block that occurred along the eastern margin of North America (Rogers and Santosh 2002; Fig. 1a), (ii) India and North China craton occurred close to each other along the western margin of East Antarctica and that the Trans-North China Orogeny was linked to Central Indian Tectonic Zone (Zhao et al. 2002), Fig. 1b), (iii) closely associated North China Craton and India occurred along the western margin of North America (Hou et al. 2008; Fig. 1c). However, none of the models address the nature of the tectonic boundary at the northern margin of NICB due to a lack of well-constrained *P-T-t* conditions of tectonic events related to supercontinent assembly.

The present study is based on a comprehensive set of geochemical data from Paleoproterozoic granites and SHRIMP geochronology: It aims at establishing *P-T* conditions of granite emplacement and probable *P-T* conditions for magma generation from the Wangtu Gneissic Complex, Sutlej Valley. These data will augment the Paleoproterozoic tectonic evolution of the north-Indian continental margin.

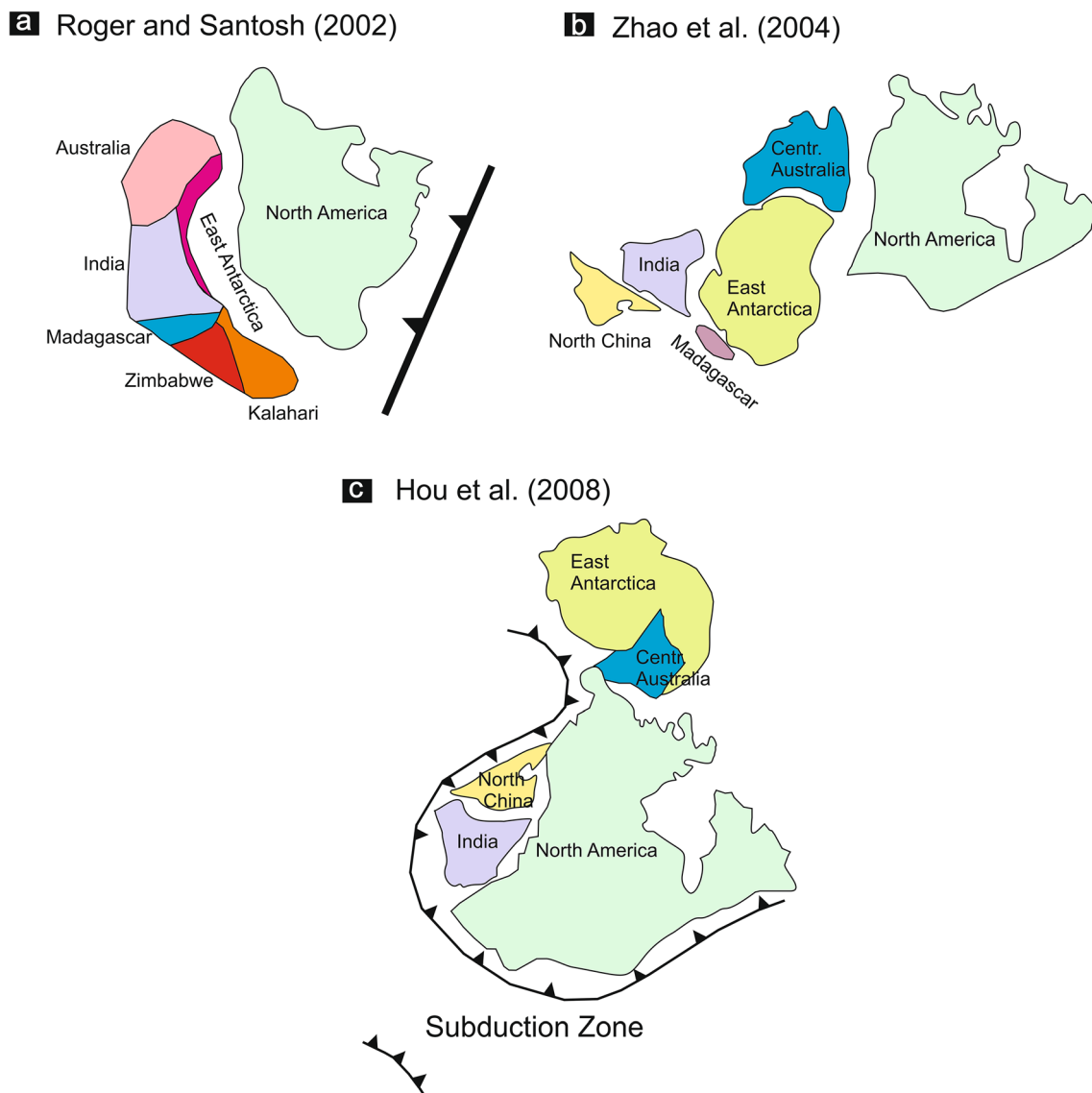


Fig. 1 a-c Different configurations of Paleoproterozoic supercontinent Columbia after Roger and Santosh (2002), Zhao et al. (2002), and Hou et al. (2008), respectively

Geological setting

General geology of Himalaya

The Himalaya in India's north-east is one of the world's active and youngest orogenic mountain belts (Fig. 2). A spectacular assemblage of metasedimentary and meta-igneous/volcanic rock exposed in the Himalayan range preserves the Precambrian to recent P - T - t evolutionary history lower-middle crustal rocks during the repeated continental collision (Fig. 2). Gansser (1964); Windley (1985); and Valdiya (2016) suggested a threefold lithodemic classification of the Himalayas from south to north, namely the Lesser Himalayas (LH), the Higher Himalayan (HH) crystallines, and the Tethyan Zone (TZ). The LH rocks are separated from the sub-Himalayan Miocene-Pliocene molasse deposits by the

Main Boundary Thrust (MBT). The Main Central Thrust (MCT and its equivalents) separate the LH and HH rocks. The HH rocks are bound to the north by the Tibetan Detachment system, north of which lies the Tethyan series (TS) marine sediments. The higher and lower Himalayan sequences are distinct lithodemic units in the Himalayan orogens, and the high-grade HH rocks are sandwiched between the low-grade LH and TS rocks in the south and north, respectively (Chakrabarti 2016; Valdiya 2016).

Ahmad et al. (2000) identified an intra-formational thrust in the LH rocks from the western Himalaya that separate the fossiliferous rocks of inner lesser Himalaya (1900–1600 Ma) from the Cambrian fossiliferous rocks of the outer Lesser Himalaya (~ 500 Ma, summarized in Richards et al. 2005). Le Fort (1975); Brookfield (1993); Upreti (1999); Gehrels et al. (2006); Saha (2013), and Larson et al. (2019) suggested

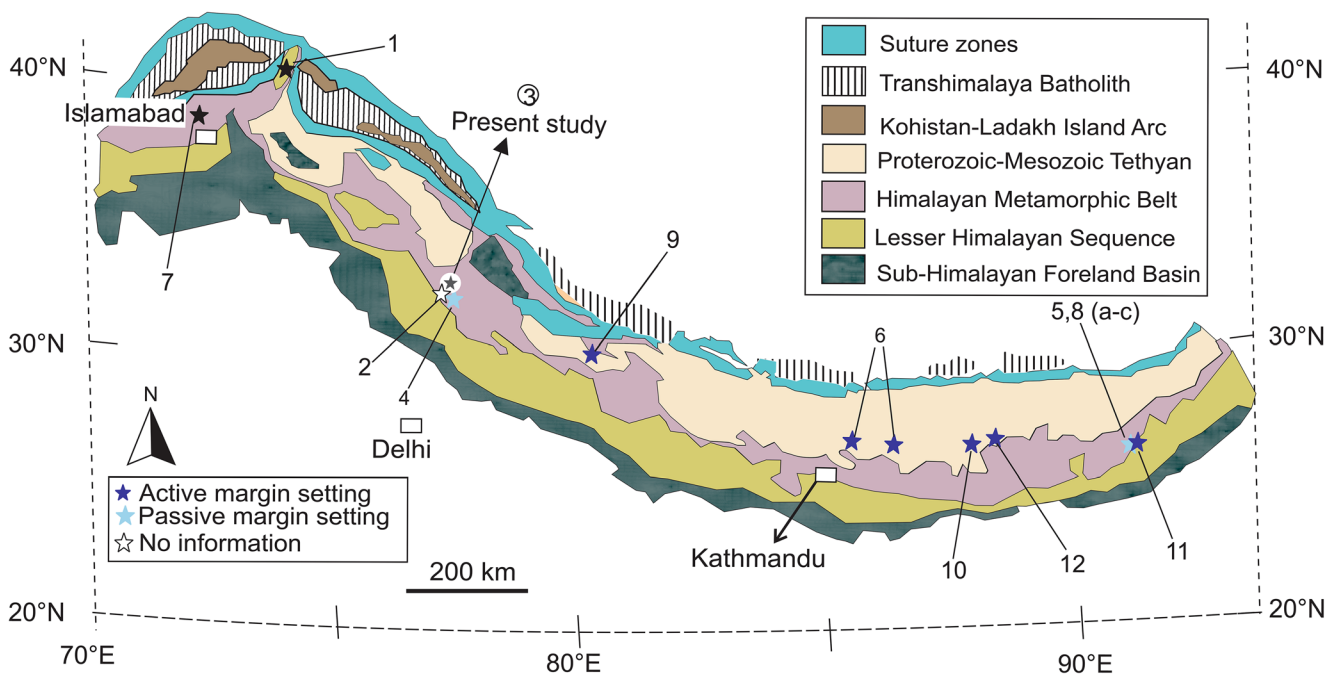


Fig. 2 Generalized geological map of Himalaya showing the distribution of Proterozoic granitoids represented by a star (modified after Yin, 2006; French et al. 2008; Singh et al. 2009; Kohn et al. 2010). The corresponding radiometric emplacement ages are given in Table 1

that the protoliths of LH metasedimentary rocks represent a basal sequence that was deposited on the passive margin of the northern extremity of the Indian peninsula. The HH rocks represent an ensemble of high-grade metamorphic rocks and granites that were emplaced between 680 and 480 Ma (Singh 2020). Valdiya (2016) suggested an intra-basinal marginal thrust (MCT) separates the lower grade HH rocks from the higher grade HH rocks. Jain and Manickavasagam (1993; Harrison et al. (1997) interpreted MCT as several hundreds of kilometer-wide high-strain zones that developed a wide range of *P-T* conditions during the Himalayan orogeny.

Basic volcanic and granites intruded the LH rocks at various stratigraphic levels (Kohn et al. 2010). The mafic-volcanic bodies are similar in compositions to basalts generated in a plume setting (Bhat et al. 1998; Ahmad et al. 1999; Ahmad 2008). Bhat and Le Fort (1992) reported Sm-Nd whole rock isochron, 2509 ± 94 Ma from basic volcanics exposed in the Kulu-Rampur area, western Lesser Himalaya. Bhat and Le Fort (1992) Bhat et al. (1998); Ahmad et al. (1999), and recently Larson et al. (2019) correlated mafic volcanism with rifting in the North Indian continental crust during Archean-Proterozoic transitions. Singh and Jain (2003) and Singh et al. (2003, 2009) identified the 2000–1800 Ma granites from the western Lesser Himalaya as within plate A-type granites that were emplaced during the rise of a Proterozoic mantle plume in a rift-related tectonic setting. In a contrasting view, Miller et al. (2000); Richards et al. (2005, 2006); Kohn et al. (2010); Phukon et al. (2018), and Pathak and Kumar (2019) suggested the existence of an extensive Paleoproterozoic arc based on the geochemical data from granites and geochronology of

zircons from granites and adjoining metasedimentary rocks from Bhutan-Arunachal, Nepal and western Lesser Himalaya.

Wangtu Gneissic Complex

The present study area lies along the Sutlej valley, Himachal Pradesh, where granitic rocks are exposed in and around Chaura, Taranda, Wangtu, and Karcham towards the north-eastern direction of amphibolite-grade meta-sediments known as the Jutogh group (Fig. 3a; Miller et al. 2000; Richards et al. 2005). Jutogh group is bounded by the Munsiri and Vaikrita thrusts. It has been variously assigned either to the Lesser Himalayan Sequences (Ahmad et al. 2000) or to the Greater Himalayan Sequence based on the metamorphic grades (Jain and Manickavasagam 1993; Singh et al. 2009). The WGC has been subject to several structural, geochemical, and geochronological studies. Jain and Manickavasagam (1993); Singh (1993); Singh et al. (2009); and Sen et al. (2013) documented two-stage folding and deformation in WGC. The first folds are mostly upright with NW-SE vergent fold closures and probably formed simultaneously with the significant Himalayan thrust forming events. The D_2 folds have a nearly orthogonal axis with the D_1 folds and formed during late- Cenozoic events.

Initially, the WGC rocks have been classified to be with peraluminous-meta aluminous chemical signature (Rao et al. 1991, 1995; Singh et al. 2009). Sen et al. (2013) documented the variation in the chemical composition in WGC. They suggested that the chemical composition of WGC locally resembles I-type granite, although a significant portion of the same

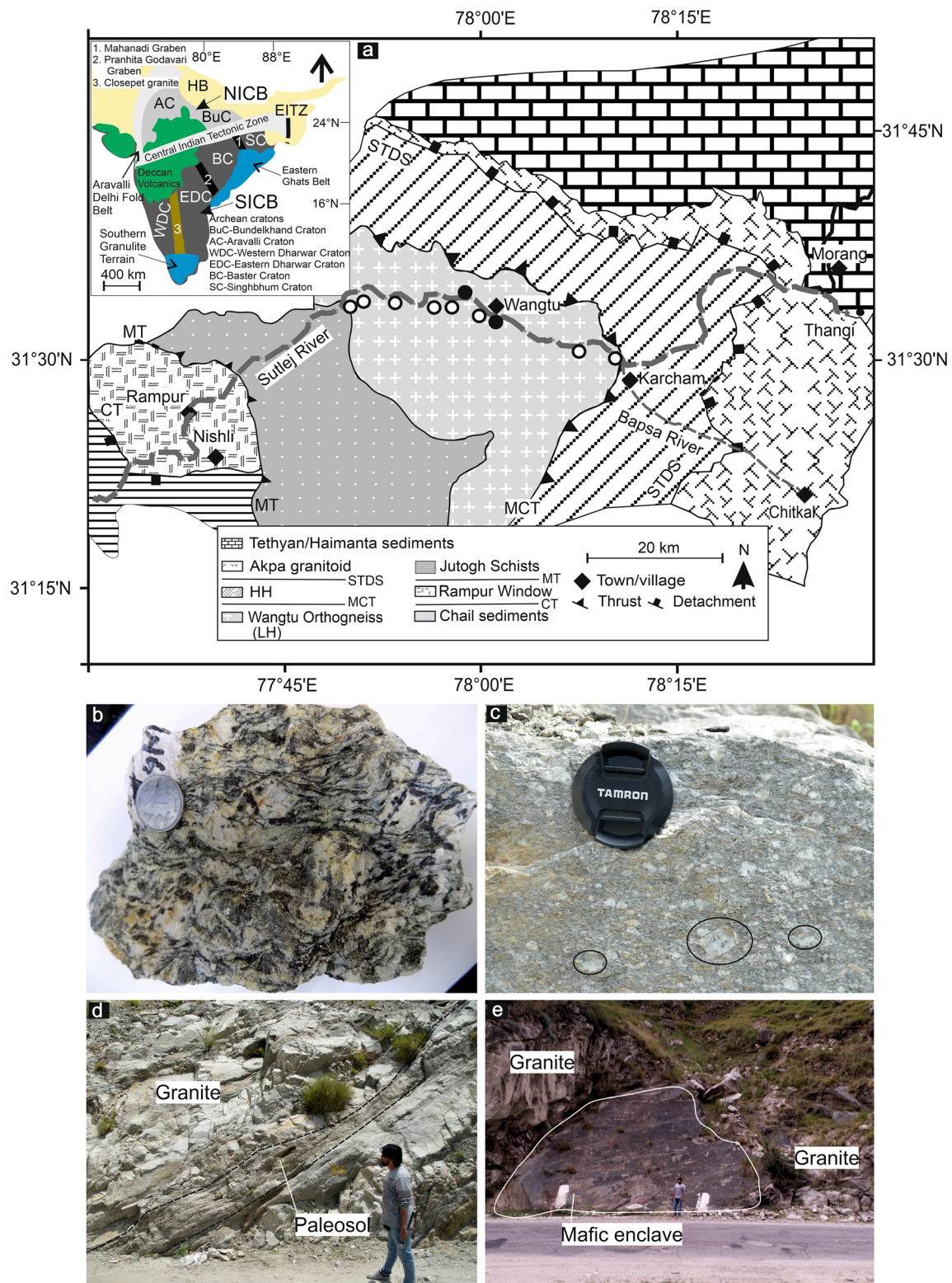


Fig. 3 **a** Generalized lithological map of Wangtu Gneissic Complex (WGC, after Vannay and Grasemann 1998) with modification from authors own field observation. The red and black filled circles mark the sample locations. Black circles represent samples used for the SHRIMP study; **b** Field photograph showing clasts of plagioclase feldspar and quartz, which impart the rock's leucocratic appearance; **c** Hand specimen of porphyroclastic granitic gneiss near Karcham area where

the biotite flanks the undeformed clasts; **d** paleosol (schist) and quartzite horizon within the WGC; **e** Mafic enclaves within the WGC. HHCS = Higher Himalayan Crystalline Sequence; LHCS = Lesser Himalayan Crystalline Sequence; LHS = Lesser Himalayan Sequence; STDS = South Tibetan Detachment System; MCT = Main Central Thrust; MT = Munsiri Thrust; CT = Chail Thrust

resembles S-type granite of Chappell and White et al. (2001). Singh et al. (2009) reported U-Pb zircon ages of 1866 ± 64 Ma with a single point U-Pb analysis that yield an older age of ~ 3000 Ma from the WGC. Miller et al. (2000) obtained a Pb-Pb evaporation age of 1840 ± 16 Ma and 1800 ± 13 Ma from meta-rhyodacites and metabasalts, respectively, from the Kullu-Rampur Window. A much younger Ar-Ar age of 9.3 ± 0.3 Ma from biotite probably marked the doming of WGC during the Himalayan orogeny (Tripathi et al. 2012; Sen et al. 2013). Pant et al. (2006) reported a Paleoproterozoic metamorphic field gradient preserved in the Jutogh metasediments in the Jeori-Rampur-Wangtu section. The Paleoproterozoic contact metamorphism is correlated with the emplacement of 1800 Ma granites adjacent to the Jutogh metasediments.

Samples and analysis

Sample description

The studied samples were collected from the Wangtu Dam, Sutlej Valley. They consist of medium- to coarse-grained, porphyroclastic granitic gneiss (Fig. 3a). K-feldspar, plagioclase feldspar, and quartz are the major porphyroclast that impart a leucocratic appearance to the rock (Fig. 3 b, c). Locally biotite and hornblende are present as accessory minerals. Biotite flakes warp around the undeformed feldspar porphyroclasts (Fig. 3c). The WGC contains numerous xenoliths of highly foliated rocks and paleosol horizons (Fig. 3d). Several mafic dikes intruded into the WGC (Fig. 3e).

Sample preparation

Powdered whole rock from each sample was used for major, trace, and rare earth analysis. The samples were cleaned by 0.01 N HCl, dried, and subsequently crushed by using a jaw breaker. After coning and quartering the crushed samples, the reduced sample was pulverized in a planetary ball mill.

The observed samples do not exhibit any distinct lineation; petrological thin sections were prepared using rock-chips cut in orthogonal directions to foliations. The rock chips were polished using silicon-carbide powder. The polished rock-chips were mounted in glass slides using Epoxies. Subsequently, the mounted chips were cut using a Buhler make Petrothin machine to achieve the desired thickness. The rough petrological thin sections were polished using micro-diamond suspension liquid.

Zircon grains were separated from sieved whole-rock powder using hydraulic, magnetic, and heavy liquid techniques and were finally handpicked under a binocular microscope. Selected grains were mounted in epoxy together with FC1 (Duluth gabbroic anorthosite, 1099 Ma; Paces and Miller 1993) and SL13 (Sri Lankan gem zircon; $U = 238$ ppm)

reference zircon samples, and ground and polished to expose internal textures. Before analysis, the grains were inspected under an optical microscope and photographed.

Analytical details

Major element oxides were analysed using a Phillips MagiX PRO Model 2440 X-ray fluorescence (XRF) spectrometer. Pressed pellets were prepared by weighing 2 g of finely powdered samples and standards in collapsible aluminum cups filled at the bottom with 2.5 g of boric acid. The cup and the powdered samples/standards were pressed under a hydraulic pressure of 25 t to obtain the pellet. International rock reference materials from the United States Geological Survey (USGS) and the Geological Survey of Japan were used to construct major elements' calibration curves. Simultaneously, the pressed pellets of samples and geochemical reference materials were loaded and analysed to control the analysis's accuracy (Krishna et al. 2007). The precision and accuracy of the analysis were 2% relative standard variation (RSD) for almost all the major oxides.

Trace-element concentrations were determined using inductively coupled plasma-mass spectrometry (ICP-MS) analysis, following the protocol of Satyanarayanan et al. (2018). For trace and rare earth elements (REE), solutions from the homogenized powder were dissolved in reagent grade HF:HNO₃ acid mixture in Savillex screw-top vessels. 25 ml Savillex Teflon pressure decomposition vessels were weighed with an aliquot (0.05 g) of the homogenized powdered sample. 10 ml of an acid mixture (containing 7:3 HF:HNO₃) was added to each sample. ¹⁰³Rh solution (0.5 ml of 10 mg/mL) was added to each sample as an internal standard. The vessels were tightly closed and kept on a hot plate at ~ 140 °C for 48 h after complete swirling. The solution was evaporated to incipient dryness after adding 1 mL of HClO₄ to ensure complete HF removal from the mixture. The residue was dissolved by adding ultra-distilled water in 20 ml of 1:1 HNO₃ and brought to a final volume of 250 ml. The sample batch was prepared with the geochemical certified reference material JG-1A along with a couple of blanks. Solutions were analyzed using a Nu Instruments Attom high resolution inductively coupled mass spectrometry (HR-ICP-MS) system operated in jump-wrapping mode at a moderate resolution of 300, which allowed us to measure precisely all analytes of interest. A solid-state 1.6 KW radio frequency (RF) generator running at 27.12 MHz was used by the ICP source. A software program is used for RF matching and tuning of the torch box. Mass flow controllers were used to getting a stable plasma gas control. The operating parameters include 4313 V for focus lens voltage, 2990 V extraction lens voltage, Ar flow rates of 1.076 L/min for samples and 0.9 L/min for Auxiliary flow, and 1300 W forward and reflected power (1300 W). Parameters were optimized carefully for maximum sensitivity

and accuracy. The instrument tuning was performed using one ng/mL multi-element (Li, Be, Mg, Sc, Co, Y, In, Cs, Tb, Tm, Pb, U). The precision and accuracy are better than 3% RSD for most of the measured elements.

Back-scattered electron (BSE) images were obtained by means of a ZEISS Gemini scanning electron microscope (SEM) operated at 20 kV and 478 pA. Silicate minerals of WGC samples were analyzed using a CAMECA SX-100 electron probe micro-analyser (EPMA). The following analytical conditions were applied: accelerating voltage 15 kV, beam current 15 nA, and beam diameter 1–5 μm . A LaB₆ cathode was used. The following reference materials were used for calibration: MgO for Mg, apatite for Ca, haematite for Fe, rhodonite for Mn, orthoclase for K, rutile for Ti, albite for Na and Si, and almandine for Al.

BSE and cathodoluminescence (CL) images of zircon grains were acquired using a JEOL (JSM 6610) SEM. The accelerating voltage is set to 15 kV and the beam size to 60 μm . For the SHRIMP analysis, a 2.5–2.8 nA mass filtered O₂⁻ primary beam was focused to a spot of approximately 25 μm diameter on the polished surface of the target zircon grain. Each spot was rastered with the primary beam for about 2 min before the analysis and then analyzed five cycles with a single electron multiplier. During one cycle, the magnet was stepped through nine peaks of ⁹⁰Zr¹⁶O (counting time = 2 s), ²⁰⁴Pb (10 s), ²⁰⁶Pb (10 s), ²⁰⁷Pb (20 s), ²⁰⁸Pb (5 s), ²³⁸U (5 s), ²³²Th¹⁶O (2 s) and ²³⁸U¹⁶O (2 s) and 204.1 (10 s; background-position). Data processing was conducted using SQUID 2.50 (Ludwig 2009) and the Concordia plots produced using Isoplot 3.75 (Ludwig 2012) programs, running under Excel 2003. Weighted mean ages of zircon were calculated using ²⁰⁷Pb-corrected ²⁰⁶Pb/²³⁸U ratios after excluding outliers under statistical t-test and reported at 95% confidence. Correction for common Pb was done using the ²⁰⁷Pb (for dates <1000 Ma) or ²⁰⁴Pb (for dates >1000 Ma) methods, respectively, based on the model by Stacy and Kramers (1975).

Data generation

Since garnet is notably absent in the studied samples, frequently cited net-transfer and exchange reactions could not be utilized to determine the *P-T* conditions for granite emplacement. Nevertheless, the peak temperature is estimated using empirical expressions involving zircon saturation in silicate melt (Gervasoni et al. 2016) and compared temperature calculated using thermodynamic expressions involving Ti incorporation in biotite (Henry et al. 2005; Wu and Hongxu 2014).

P-T pseudosection is also constructed using PERPLEX (Connolly 2009) to constrain the magmatic assemblages' *P-T* conditions in granites. Thermodynamic data of mineral phases are adapted from Holland and Powell (2011) and its subsequent modifications (hp633ver.dat). The activity-composition relationships for plagioclase, melt, biotite, white

mica are adopted from Newton et al. (1980); Holland and Powell (2001); Coggon and Holland (2002); and Tajčmanová et al. (2007), respectively, for calculating the phase-relationship in granite. As biotite and K-feldspar are present in the studied samples, the amount of H₂O is adjusted from biotite's modal abundances in the studied samples. In the first step, ten petrological thin sections of granites were scanned in a SEM to estimate the relative proportion of biotite compared to K-feldspar. Since biotite and K-feldspar are only minerals to contain K₂O as a major component, and plagioclase feldspar is likely to contain K₂O < 1 wt%, the total K₂O content in the studied sample is adjusted based on the relative modal abundances of biotite and K-feldspar. As the maximum amount of volatiles (OH, F) present is twice to cations (K, Na, and Ca) present in the I site of ideal biotite stoichiometry (Deer et al. 2013), the reallocated molar K₂O for biotite is doubled to estimate the minimum amount of H₂O, required to stabilize biotite with predicted abundances similar to the amount of biotite present in the studied samples. The molar albite fraction of plagioclase [(Na/Na + Ca + K) X100] and Fe# of biotite [(Fe/Fe + Mg) X100] was calculated to constrain the *P-T* conditions of granites.

Generally, the magma generated from the partial melting of lower crust and mantle ascent upward to cool down and crystallize magmatic phases. Thus, the emplacement *P-T* conditions may not be similar to the *P-T* conditions at which magma was generated. Since S-type granites are mostly derived from sedimentary sources (Chappell and White 2001), the adjoining Jutogh metasediments' chemical composition is approximated for the source materials for the present study (Chambers et al. 2008). The thermodynamic data and minerals solution models for garnet, staurolite, biotite, mica, cordierite, plagioclase, and melt are adapted from the activity-composition relationship defined specifically for metapelite by White et al. (2007) to model phase relations in Jutogh metasediments. Quartz is assumed to be excess. As mica and biotite are the abundant hydrous minerals in metapelites, the H₂O is adjusted for just-saturation for mica and biotite stabilization. The modal abundances of silicate phases, and weight fractions of SiO₂, Na₂O + K₂O, and Al₂O₃/(Na₂O + K₂O), were modeled to constrain the *P-T* conditions for magma generation. In all the calculations, all Fe is assumed to be Fe²⁺ that may lead to a pseudo-stabilization of garnet in the computed phase diagrams (White et al. 2000; Tinkham et al. 2003).

Results

Geochemistry

A summary of the geochemical analysis of ten representative samples from WGC is given in Table 1. Results of

geochemical analysis of individual samples are provided in Table S1 in electronic supplementary material (ESM). The studied granites are calc-alkaline in composition (Fig. 4a; Irvine and Baragar 1971). The SiO₂ and Al₂O₃ content of the studied sample varies between 69 and 72 wt% and 13–15 wt%, respectively. The Fe₂O₃ content of the same samples varies between 2 and 6 wt%. In contrast to higher Fe₂O₃ content, the granites are poor in MgO content (0.5–2.5 wt%). Regarding the alkali element content, the Na₂O and K₂O vary between 2.16–3.11 wt% and 4.13–6.21 wt%, respectively, with K₂O/Na₂O ratio between 1.5–3.3. The CaO content is variable between 1.0–2.5 wt%. The TiO₂ and P₂O₅ content are <1 wt%.

In the total alkali versus silica diagram (Middlemost 1994), data obtained from the samples studied herein plot between the quartz-monzonite and granite fields (Fig. S1a in ESM). The A/CNK of the studied samples is scattered between 0.94–1.54, with an average value of 1.20. Accordingly, in an A/CNK versus SiO₂ plot, a majority of the samples with A/CNK > 1.0 concentrate in the peraluminous field resembling S-type granites, although a small set of samples with A/CNK < 1.0 concentrate in the meta-aluminous area resembling I-type granite (Fig. 4b). In a K₂O versus SiO₂ plot, the studied samples are classified as shoshonite (Fig. S1b in the ESM). The scattered A/CNK values of the studied samples probably indicate variable sources for the origin of WGC.

In a primitive mantle normalized trace element plot (McDonough and Sun 1995), the WGC is characterized by a positive K anomaly and a negative Nb-Ti-Ta- anomaly (Fig. 4c). The total REE content (REEs) of studied samples varies between 157.48–491.36. In an REE normalized spider

diagram (McDonough and Sun 1995), the (La/Lu)_N and La_N/Sm_N vary in the ranges 7.72–21.63 and 2.63–5.02, respectively, with pronounced negative Eu anomaly (Table S1 in the ESM, Fig. 4d) (Table 2).

Petrography and mineral chemistry

In-situ mineral chemical analysis of representative samples is given in Tables 3, 4 and 5. K-feldspar, plagioclase, and biotite are the major minerals in the studied samples. Zircon, apatite, and iron-oxides (hematite) occur as accessory phases. The central part of WGC is mostly undeformed, although the intensity of deformation increases towards HH-WGC contact in the north near Karcham. In the relatively undeformed variety, plagioclase (*ab* mol% = 70–78), K-feldspar (*Or* mol% = 85–90) occur porphyroblast in a moderately fine-grained groundmass of K-feldspar and quartz. Plagioclase grains are mostly tabular (average grain size ~50–75 μm), undeformed, and exhibit lamellar twins. Spindle-shaped deformation band and twin-lamellae are notably absent in plagioclase. Quartz grains are relatively coarser (average diameter ~200 μm) and exhibit wavy grain boundaries, chessboard twinning, and undulose extinction. Discontinuous biotite flakes (Mg# = 28–30) wrap the porphyroblasts. In the plagioclase rich domains, the biotite flakes are mostly parallel to the lamellar twin lamellae. The Fe# and TiO₂ of biotite vary between 70 and 73 and 2.89–3.83 wt%, respectively. Myrmekite occurs at the plagioclase and K-feldspar grain boundary. White-mica is mostly muscovite with Si between 3.01–3.02 apfu (based on 11 O atoms per formula unit).

Table 1 Available geochronological information for Paleoproterozoic magmatism across the Himalayas

Serial	Location	Age (in Ma), Methodology, References
1	Iskere orthogneiss	1852±14, <i>U-Pb Zr</i> , Zaitler et al. (1989)
2	Magladgad granite stock	2068±5, <i>U-Pb Zr</i> , Singh et al. (1993)
3	Wangtu gneissic Complex, Himachal Himalaya	1868±6, 2487±20, <i>U-Pb Zr</i> , present study
4	Wangtu granite, Sutlej Valley, Himachal Himalaya	1866±10, <i>U-Pb Zr</i> , Singh et al. (1993), 1865±4, <i>U-Pb Zr</i> , Singh et al. (2009)
5	Bomdila gneiss	1874±24, <i>U-Pb Zr</i> , Rao (1988)
6	Granite orthogneiss and augen gneiss from Nepal Himalaya	1832±23, 1878±11, <i>U-Pb Zr</i> , 1780±23, 1791±12, <i>U-Pb Zr</i> , Kohn et al. (2010)
7	Besham gneiss, Shang gneiss, Pakistan	1880±24, 1864±4, <i>U-Pb Zr</i> , Dipietro and Isachsen (2001)
8(a-c)	Lumla/Dirang Formation, Bomdila gneiss	1600, 1743±4, <i>U-Pb Zr</i> , Yin et al. (2006, 2010a), Saha (2013)
9	Munsiari augen gneiss, chiplakot crystalline belt, Kumayun Himalaya	1954.9±7.3, 1972.3±4.0, <i>U-Pb Zr</i> , Phukon et al. (2017)
10	Daling Group from Rangit window Darjeeling-Sikkim Himalaya	~1850 (<i>Ar-Ar</i>), Acharya (2017)
11	Bodmdila granite gneiss western Arunachal Himalaya	1752±23, <i>U-Pb Zr</i> , Pathak and Kumar (2019)
12	Lingtse gneiss Sikkim Himalaya	1834±37, 1853±19, <i>U-Pb Zr</i> , Mottram et al. (2014)

Sample localities are shown in Fig. 2

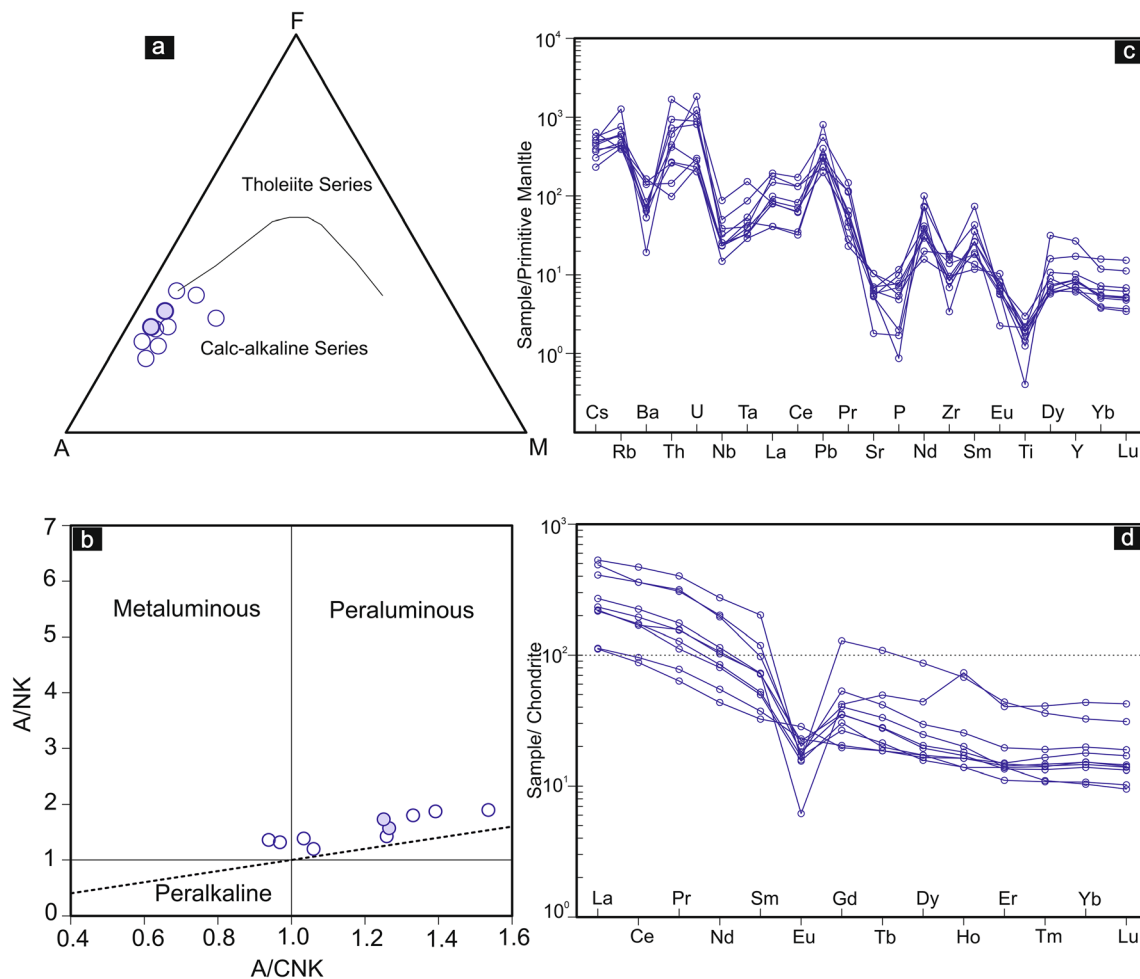


Fig. 4 Geochemical classification diagram for WGC samples. **a** A (Na₂O + K₂O) – F (FeOⁱ) – M (MgO) triangular diagram (after Irvine and Baragar 1971); **b** A/CNK – A/NK bivariate plot after Shand (1943), discriminating metaluminous, peraluminous, and peralkaline compositions; **c-d** Primitive mantle normalized trace elements variation

diagram, and chondrite normalized rare-earth element plots for WGC samples, respectively. Normalization factors are from Sun and McDonough (1995). Shaded symbols represent samples used for geochronological studies

***P-T* conditions for magma emplacement**

Single element thermometers

The Ti saturation in magmatic zircon yields crystallization temperature $\sim 650\text{--}750\text{ }^{\circ}\text{C}$ (Fig. 5a). The TiO₂, FeO, and MgO content of biotite from the studied sample point towards the magmatic origin (Fig. 5b, Nachit et al. 2005). The TiO₂ content and Mg# of biotite yield temperature $680\text{ }^{\circ}\text{C} \pm 50\text{ }^{\circ}\text{C}$, between a pressure range of 0.4–0.6 GPa (Henry et al. 2005). Empirical formulations after Wu and Hongxu (2014) estimate temperature $\sim 700 \pm 50\text{ }^{\circ}\text{C}$ and $850\text{ }^{\circ}\text{C} \pm 50\text{ }^{\circ}\text{C}$ at pressure 0.5 GPa and 1.2 GPa, respectively (Fig. S2 in the ESM).

***P-T* pseudosection analysis**

The phase topology constructed for the WGC sample (WG-49B) between temperature 600–900 °C and pressure 0.5–

1.4 GPa is shown Fig. 6a. In the *P-T* pseudosection, the assemblage plagioclase+biotite+mica+san + melt is stable at temperature $< 700\text{ }^{\circ}\text{C}$ for pressure 0.5–1.4 GPa. An increase in temperature $> 800\text{ }^{\circ}\text{C}$ leads to the destabilization of biotite by stabilizing garnets and sillimanite. Since the studied sample does not contain garnet or sillimanite, the “*garnet-in*” and “*sillimanite-in*” marked the maximum pressure and temperature the rock has experienced. Figure 6b shows the modeled chemical parameters for plagioclase and biotite. The modeled ab mol% isopleths have a relatively shallow slope with an increasing value towards higher pressure. The modeled Fe# of biotite has a steep slope with an increasing Fe# towards higher temperatures. The intersection of modeled compositional isopleths corresponding to the measured composition intersects at temperature $\sim 700\text{ }^{\circ}\text{C}$ and pressure $\sim 1.0\text{--}1.1\text{ GPa}$. Thus, the *P-T* conditions obtained from isopleth thermobarometry correspond to a geothermal gradient of $750\text{ }^{\circ}\text{C}/\text{GPa}$ (Brown 2008).

Table 2 Major oxides, trace and rare-earth-elements content, of representative WGC samples (number of samples =10)

Major oxides (wt%)	
SiO ₂	74.59 - 68.83
Al ₂ O ₃	15.96 - 13.68
Fe ₂ O ₃	5.05 - 2.21
MnO	0.05 - 0.01
MgO	2.59 - 0.31
CaO	2.55 - 0.75
Na ₂ O	3.17 - 1.63
K ₂ O	7.01 - 4.13
TiO ₂	0.60 - 0.08
P ₂ O ₅	0.24 - 0.02
Trace elements (ppm)	
Sc	13.20 - 4.40
V	33 - 5
Cr	478 - 46
Co	8 - 4.10
Ni	10.50 - 6.00
Cu	5.30 - 1.30
Zn	552 - 24
Ga	38 - 16
Rb	763 - 235
Sr	207 - 36
Y	116 - 26
Zr	191 - 36
Nb	58 - 10
Cs	439 - 64
Ba	1092 - 127
Hf	5.80 - 1.10
Ta	5.63 - 1.08
Pb	120.90 - 29.80
Th	135 - 7.80
U	36.90 - 4.10
Rare-earth-elements (ppm)	
La	126 - 26
Ce	288 - 54
Pr	37 - 6
Nd	125 - 20
Sm	29.90 - 4.80
Eu	1.60 - 0.35
Gd	25.70 - 3.90
Tb	3.93 - 0.67
Dy	21.40 - 3.90
Ho	4 - 0.76
Er	7 - 1.80
Tm	1.01 - 0.27
Yb	7 - 1.70
Lu	1.04 - 0.23

Magma parental to the S-type granite originate due to the partial melting of the supracrustal rocks that have been developed through one or more cycles of weathering of the parental rocks (Chappell and White 2001). Chambers et al. (2008) document a Paleoproterozoic (1810 Ma) crustal anatexis in the Jutogh metasediments. On a similar approach, several researchers, e.g., Chambers et al. (2008); Kohn et al. (2010), suggested the melting of metapelites to explain the origin of Paleoproterozoic S-type granites in the LH. However, none of the authors address the degree of partial melting of metapelites and the *P-T* conditions of magma generation. Thus, to address the physical conditions of magma generation, the melting of the averaged whole-rock chemical compositions of Jutogh metapelite (Chambers et al. 2008) is modeled using PERPLEX (Connolly 2009).

The phase topology for the Jutogh metasediments in the temperature range of 600–1000 °C and pressure 0.5–1.4 GPa is shown in Fig. 7a. The *P-T* pseudosection is divided into three distinct domains, i.e., *HP-LT* kyanite bearing domains, *HT-HP* sillimanite bearing domains, and *HT-LP* cordierite bearing domains. In the sillimanite bearing domains, the assemblage mica-biotite-plagioclase-sillimanite-staurolite (Pant et al. 2006) is stable in a narrow field at temperature < 650 °C, pressure 0.6–0.7 GPa. Staurolite is unstable with a change in *P-T* conditions, and mica-biotite-plagioclase-sillimanite (without staurolite) becomes stable at temperature > 650 °C, between pressure 0.5–0.7 GPa. Similarly, an increase in pressure > 0.7 GPa at temperature < 650 °C leads to the stabilization of mica-biotite-plagioclase-kyanite-garnet (without melt and staurolite).

Silicate melt appears as a stable phase at temperature 700 °C, pressure 0.5 GPa to temperature 750 °C, pressure 1.4 GPa. The subsequent increase in temperature lead to the subsequent destabilization of mica and biotite between temperature 750–850 °C. Finally, garnet, sillimanite, and rutile-ilmenite coexist with silicate melt at temperature > 900 °C between pressure 0.5–1.4 GPa.

The modal abundances of the minerals are shown in Fig. 7 b-d. The muscovite modal abundance increases with an increase in pressure in the kyanite domain and decreases with an increase in temperature in the sillimanite domain. The biotite and feldspar abundances decrease with an increase in pressure. The modal abundances for melt and garnet increase with an increase in temperature. The opposite trends for muscovite, biotite, plagioclase and melt, garnet imply melting of hydrous phases (biotite, muscovite) and plagioclase leading to silicate melt and garnet formation with an increase in temperature.

The *P-T* conditions of melt generation are further constrained by constraining the chemical composition of silicate melt (Fig. 7 e-f). The SiO₂ (wt%) of silicate melt increases with an increase in temperature. Similarly, the Na₂O + K₂O (wt%) of the melt increases with an increase in temperature. The intersection of modelled isopleths having values similar

Table 3 Chemical compositions (EPMA results), calculated mineral formulae and calculated end-member fractions for plagioclase and K-feldspar from representative WGC samples

Sample	WG-49B			WG-86A			WG-49B			WG-86A										
	Plagioclase			Plagioclase			K-feldspar			K-feldspar										
Major oxides (wt%)																				
SiO ₂	62.52	63.31	63.53	62.75	63.49	59.67	59.44	61.09	59.73	59.45	63.99	64.25	64.88	64.05	64.80	64.53	64.27	64.14	64.37	64.30
TiO ₂	0.02	0.02	0.01	0.01	0.01	0.01	0.01	0.00	0.00	0.00	0.00	0.00	0.00	0.00	0.00	0.01	0.00	0.00	0.00	0.00
Al ₂ O ₃	23.45	23.67	23.29	23.68	23.58	25.47	25.86	24.99	25.23	25.65	18.44	18.54	18.66	18.58	18.89	18.66	18.85	18.79	19.12	18.85
Cr ₂ O ₃	0.00	0.00	0.00	0.00	0.00	0.00	0.00	0.02	0.00	0.00	0.00	0.00	0.00	0.00	0.00	0.00	0.00	0.00	0.00	0.00
Fe ₂ O ₃	0.00	0.00	0.00	0.00	0.00	0.00	0.00	0.00	0.00	0.00	0.00	0.00	0.00	0.00	0.00	0.00	0.00	0.00	0.00	0.00
FeO	0.15	0.05	0.20	0.12	0.00	0.10	0.00	0.06	0.23	0.00	0.00	0.10	0.00	0.25	0.00	0.00	0.00	0.04	0.07	0.00
MnO	0.00	0.00	0.04	0.00	0.00	0.00	0.05	0.00	0.00	0.00	0.12	0.03	0.00	0.00	0.04	0.03	0.08	0.04	0.00	0.00
MgO	0.03	0.01	0.00	0.00	0.00	0.00	0.00	0.01	0.00	0.00	0.01	0.02	0.03	0.00	0.00	0.02	0.00	0.00	0.00	0.00
CaO	4.10	4.16	3.77	4.22	4.06	7.06	6.96	6.03	6.76	7.26	0.00	0.00	0.00	0.00	0.00	0.00	0.00	0.00	0.01	0.00
Na ₂ O	8.79	9.19	9.82	9.66	9.58	7.43	7.53	7.66	7.59	7.31	1.23	1.20	1.15	1.23	1.28	1.64	1.25	1.13	1.09	1.20
K ₂ O	0.26	0.34	0.26	0.22	0.14	0.25	0.28	0.29	0.26	0.25	14.64	14.67	14.96	14.48	14.73	13.76	14.34	14.76	13.17	14.20
Total	99.32	100.75	100.92	100.66	100.86	99.99	100.13	100.15	99.80	99.92	98.43	98.81	99.93	98.34	99.74	98.65	98.79	98.90	97.84	98.55
Calculated mineral formulae (apfu)*																				
Si	2.781	2.780	2.788	2.765	2.784	2.660	2.648	2.707	2.668	2.653	2.990	2.989	2.987	2.990	2.985	2.993	2.984	2.981	2.992	2.988
Ti	0.001	0.001	0.000	0.000	0.000	0.000	0.000	0.000	0.000	0.000	0.000	0.000	0.000	0.000	0.000	0.000	0.000	0.000	0.000	0.000
Al	1.230	1.225	1.205	1.230	1.219	1.339	1.358	1.305	1.328	1.349	1.016	1.017	1.013	1.022	1.026	1.020	1.032	1.030	1.048	1.033
Cr	0.000	0.000	0.000	0.000	0.000	0.000	0.000	0.001	0.000	0.000	0.000	0.000	0.000	0.000	0.000	0.000	0.000	0.000	0.000	0.000
Fe ³⁺	0.006	0.002	0.007	0.004	0.000	0.004	0.000	0.002	0.009	0.000	0.000	0.004	0.010	0.000	0.000	0.000	0.000	0.002	0.003	0.000
Fe ²⁺	0.000	0.000	0.000	0.000	0.000	0.000	0.000	0.000	0.000	0.000	0.000	0.000	0.000	0.000	0.000	0.000	0.000	0.000	0.000	0.000
Mn	0.000	0.000	0.001	0.000	0.000	0.000	0.002	0.000	0.000	0.000	0.005	0.001	0.000	0.000	0.002	0.001	0.003	0.002	0.000	0.000
Mg	0.002	0.001	0.000	0.000	0.000	0.000	0.000	0.001	0.000	0.000	0.001	0.001	0.001	0.000	0.000	0.001	0.000	0.000	0.000	0.000
Ca	0.195	0.196	0.177	0.199	0.191	0.337	0.332	0.286	0.323	0.347	0.000	0.000	0.000	0.000	0.000	0.000	0.000	0.000	0.000	0.000
Na	0.758	0.783	0.836	0.825	0.815	0.642	0.650	0.658	0.657	0.632	0.111	0.108	0.103	0.111	0.114	0.147	0.113	0.102	0.098	0.108
K	0.015	0.019	0.015	0.012	0.008	0.014	0.016	0.016	0.015	0.014	0.873	0.871	0.879	0.862	0.866	0.814	0.849	0.875	0.781	0.842
Total	4.988	5.007	5.029	5.035	5.017	4.996	5.006	4.976	5.000	4.995	4.996	4.991	4.985	4.985	4.993	4.976	4.981	4.992	4.922	4.971
Calculated end-member fractions (mol%)																				
Or	1.550	1.904	1.459	1.158	0.789	1.410	1.603	1.667	1.508	1.410	88.720	88.968	88.592	89.511	88.367	84.703	88.254	89.560	88.851	88.632
Ab	78.306	78.457	81.323	79.633	80.375	64.653	65.130	68.542	66.030	63.646	11.280	11.032	11.408	11.408	11.633	15.297	11.746	10.440	11.149	11.368
An	20.145	19.639	17.218	19.208	18.836	33.938	33.267	29.792	32.462	34.945	0.000	0.000	0.000	0.000	0.000	0.000	0.000	0.000	0.000	0.000

*Calculated based on 8 oxygen atoms per formula unit, Fe³⁺ from stoichiometry, Or: Orthoclase (K/(K+Na+Ca) × 100), Ab: Albite (Na/(K+Na+Ca) × 100), An: Anorthite (Ca/(K+Na+Ca) × 100)

Table 4 Chemical compositions (EPMA results), calculated mineral formulae and calculated end-member fractions for biotite from representative WGC samples

Sample	WG-49B																WG-86A																
Mineral	Biotite																Biotite																
Major oxides (wt%)																																	
SiO ₂	34.32	35.18	34.19	34.07	34.82	34.07	34.56	34.12	34.17	33.6	33.75	34.11	34.51	33.76	34.3	34.53	34.32	35.18	34.19	34.07	34.82	34.07	34.56	34.12	34.17	33.6	33.75	34.11	34.51	33.76	34.3	34.53	
TiO ₂	3.83	3.51	3.72	3.42	3.83	3.7	2.89	3.69	3.32	3.46	3.18	3.77	3.3	3.55	3.37	3.41	3.83	3.51	3.72	3.42	3.83	3.7	2.89	3.69	3.32	3.46	3.18	3.77	3.3	3.55	3.37	3.41	
Al ₂ O ₃	17.87	17.66	18.63	20.34	18.91	20.41	18.75	20.61	18.61	18.56	17.65	17.6	18.56	17.53	17.61	17.22	17.87	17.66	18.63	20.34	18.91	20.41	18.75	20.61	18.61	18.56	17.65	17.6	18.56	17.53	17.61	17.22	
Cr ₂ O ₃	0	0.03	0	0	0	0	0	0	0	0	0	0	0	0	0	0	0	0.03	0	0	0	0	0	0	0	0	0	0	0	0	0	0	0
Fe ₂ O ₃	0	0	0	0	0	0	0	0	0	0	0	0	0	0	0	0	0	0	0	0	0	0	0	0	0	0	0	0	0	0	0	0	0
FeO	23.9	23.87	24.63	22.48	23.64	23.29	24.25	22.7	24.42	25.17	25.45	25.19	24.67	26.32	26.03	26.3	23.9	23.87	24.63	22.48	23.64	23.29	24.25	22.7	24.42	25.17	25.45	25.19	24.67	26.32	26.03	26.3	
MnO	0.16	0.11	0.23	0.31	0.14	0.26	0.22	0.17	0.32	0.28	0.22	0.19	0.22	0.11	0.24	0.24	0.16	0.11	0.23	0.31	0.14	0.26	0.22	0.17	0.32	0.28	0.22	0.19	0.22	0.11	0.24	0.24	
MgO	5.68	6.03	5.21	5.66	5.29	5.46	5.85	5.6	5.09	5.09	5.3	5.37	5.1	5.38	4.65	4.83	5.68	6.03	5.21	5.66	5.29	5.46	5.85	5.6	5.09	5.09	5.3	5.37	5.1	5.38	4.65	4.83	
CaO	0	0	0.03	0	0.03	0	0.02	0	0	0	0.02	0	0	0.01	0	0	0	0	0.03	0	0.03	0	0.02	0	0	0	0.02	0	0	0.01	0	0	
Na ₂ O	0.18	0.16	0.18	0.13	0.21	0.18	0.09	0.18	0.06	0.12	0.09	0.09	0.15	0.13	0.15	0.14	0.18	0.16	0.18	0.13	0.21	0.18	0.09	0.18	0.06	0.12	0.09	0.09	0.15	0.13	0.15	0.14	
K ₂ O	9.21	9.47	9.29	9.26	9.34	9.23	9.39	9.15	9.24	9.24	9.36	9.27	9.22	9.2	9.23	9.19	9.21	9.47	9.29	9.26	9.34	9.23	9.39	9.15	9.24	9.24	9.36	9.27	9.22	9.2	9.23	9.19	
Totals	95.15	96.02	96.11	95.67	96.21	96.6	96.02	96.22	95.23	95.52	95.02	95.59	95.73	95.99	95.58	95.86	95.15	96.02	96.11	95.67	96.21	96.6	96.02	96.22	95.23	95.52	95.02	95.59	95.73	95.99	95.58	95.86	
Calculated mineral formulae (apfu)*																																	
Si	2.684	2.722	2.656	2.625	2.682	2.608	2.679	2.611	2.676	2.638	2.672	2.675	2.687	2.653	2.7	2.712	2.684	2.722	2.656	2.625	2.682	2.608	2.679	2.611	2.676	2.638	2.672	2.675	2.687	2.653	2.7	2.712	
Ti	0.225	0.204	0.217	0.198	0.222	0.213	0.168	0.212	0.196	0.204	0.189	0.222	0.193	0.21	0.199	0.201	0.225	0.204	0.217	0.198	0.222	0.213	0.168	0.212	0.196	0.204	0.189	0.222	0.193	0.21	0.199	0.201	
Al	1.648	1.611	1.706	1.847	1.717	1.842	1.713	1.86	1.718	1.718	1.647	1.627	1.704	1.624	1.634	1.595	1.648	1.611	1.706	1.847	1.717	1.842	1.713	1.86	1.718	1.718	1.647	1.627	1.704	1.624	1.634	1.595	
Cr	0	0.002	0	0	0	0	0	0	0	0	0	0	0	0	0	0	0	0.002	0	0	0	0	0	0	0	0	0	0	0	0	0	0	0
Fe ³⁺	0	0	0	0	0	0	0	0	0	0	0	0	0	0	0	0	0	0	0	0	0	0	0	0	0	0	0	0	0	0	0	0	0
Fe ²⁺	1.563	1.545	1.6	1.448	1.523	1.491	1.572	1.453	1.599	1.653	1.685	1.652	1.607	1.73	1.714	1.728	1.563	1.545	1.6	1.448	1.523	1.491	1.572	1.453	1.599	1.653	1.685	1.652	1.607	1.73	1.714	1.728	
Mn	0.011	0.007	0.015	0.02	0.009	0.017	0.014	0.011	0.021	0.019	0.015	0.013	0.015	0.007	0.016	0.016	0.011	0.007	0.015	0.02	0.009	0.017	0.014	0.011	0.021	0.019	0.015	0.013	0.015	0.007	0.016	0.016	
Mg	0.662	0.695	0.603	0.65	0.607	0.623	0.676	0.639	0.594	0.596	0.625	0.628	0.592	0.63	0.545	0.565	0.662	0.695	0.603	0.65	0.607	0.623	0.676	0.639	0.594	0.596	0.625	0.628	0.592	0.63	0.545	0.565	
Ca	0	0	0.002	0	0.002	0	0.002	0	0	0	0.002	0	0	0.001	0	0	0	0	0.002	0	0.002	0	0.002	0	0	0	0.002	0	0	0.001	0	0	
Na	0.027	0.024	0.027	0.019	0.031	0.027	0.014	0.027	0.009	0.018	0.014	0.014	0.023	0.02	0.023	0.021	0.027	0.024	0.027	0.019	0.031	0.027	0.014	0.027	0.009	0.018	0.014	0.014	0.023	0.02	0.023	0.021	
K	0.919	0.935	0.921	0.91	0.918	0.901	0.929	0.893	0.923	0.926	0.945	0.928	0.916	0.922	0.927	0.921	0.919	0.935	0.921	0.91	0.918	0.901	0.929	0.893	0.923	0.926	0.945	0.928	0.916	0.922	0.927	0.921	
Total	7.739	7.745	7.747	7.717	7.711	7.722	7.767	7.706	7.736	7.772	7.794	7.759	7.737	7.797	7.758	7.759	7.739	7.745	7.747	7.717	7.711	7.722	7.767	7.706	7.736	7.772	7.794	7.759	7.737	7.797	7.758	7.759	
Calculated end-member fractions (mol%)																																	
Mg#	29.80	31.00	27.40	31.00	28.50	29.50	30.11	30.50	27.10	26.50	27.10	27.50	26.90	26.70	24.10	24.60	29.80	31.00	27.40	31.00	28.50	29.50	30.11	30.50	27.10	26.50	27.10	27.50	26.90	26.70	24.10	24.60	
Fe#	70.20	69.00	72.60	69.00	71.50	70.50	69.89	69.50	72.90	73.50	72.90	72.50	73.10	73.30	75.90	75.40	70.20	69.00	72.60	69.00	71.50	70.50	69.89	69.50	72.90	73.50	72.90	72.50	73.10	73.30	75.90	75.40	

*Calculated based on 11 oxygen atoms per formula unit, Fe³⁺ from stoichiometry, Mg# (Mg/Mg+Fe)×100, Fe# (Fe/Mg+Fe)×100

to the WGC, i.e., SiO₂ = 68–70 wt%, (Na₂O + K₂O) ~ 10–8 wt% intersect at temperature 850–900 °C, and pressure 1.1–1.2 GPa. The modeled A/NK values in the predicted *P-T* window are between 1.6–1.9 and are consistent with observed A/NK values of the WGC rocks.

U-Pb zircon geochronology

Generalities

Two representative samples (WG 49B and WG-86A) that exhibit the least deformed pristine igneous assemblages are selected for U-Pb geochronological studies. The representative CL images from both the samples are shown in Fig. 8. The geochronological data are presented in Tables 6 and 7,

respectively. The ²⁰⁷Pb/²⁰⁶Pb ratio is considered for age calculation. More than >70% of data falls near Concordia for the studied samples. The age distribution of zircon varies between 2487 ± 20 Ma to 1867 ± 7 Ma of all the analyses taken together.

Sample WG-49B

A total of 21 spots, including seven core and 14 rims, are analyzed from 16 zircons separated from sample WG 49B. The size of the zircon crystals ranges between 150 and 210 μm, and the aspect ratio varies from 2:1 to 4:1. The zircons are euhedral-subhedral and preserve multifaceted prismatic crystals. In the CL images, most of the zircon grains exhibit a distinct core, overgrown by rims of variable

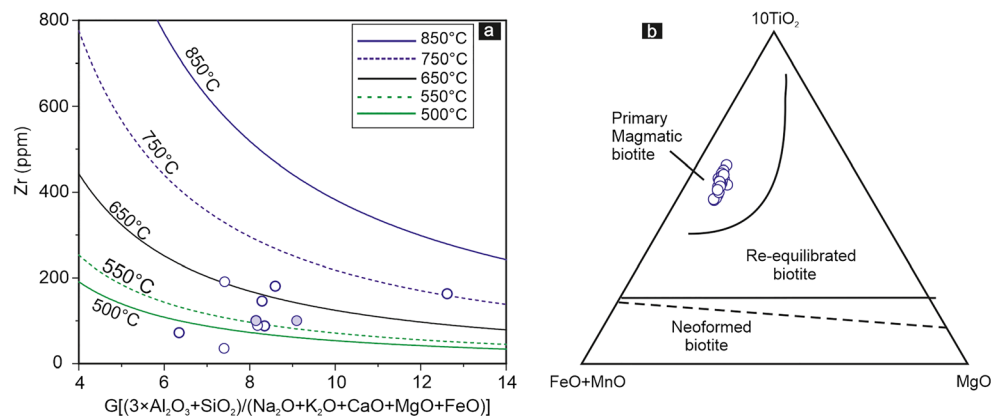
Table 5 Chemical compositions (EPMA results), calculated mineral formulae and calculated end-member fractions for muscovite and ilmenite from representative WGC samples

Sample	WG49		WG86	WG49
Mineral	Muscovite		Muscovite	Ilmenite
Major oxides (wt%)				
SiO ₂	45.65	45.69	45.70	0.00
TiO ₂	1.43	2.38	1.93	52.65
Al ₂ O ₃	35.03	33.85	35.37	0.01
Cr ₂ O ₃	0.00	0.00	0.04	0.00
Fe ₂ O ₃	0.00	0.00	0.00	0.00
FeO	2.94	2.93	2.68	44.49
MnO	0.12	0.00	0.00	2.73
MgO	1.00	1.14	0.92	0.03
CaO	0.00	0.02	0.00	0.00
Na ₂ O	0.29	0.26	0.25	0.03
K ₂ O	7.06	6.98	6.44	0.04
Totals	93.52	93.25	93.33	99.98
Calculated mineral formulae (apfu)*				
Si	3.042	3.054	3.035	0.000
Ti	0.072	0.120	0.096	0.999
Al	2.752	2.668	2.769	0.000
Cr	0.000	0.000	0.002	0.000
Fe ³	0.115	0.115	0.104	0.005
Fe ²	0.049	0.049	0.045	0.934
Mn	0.007	0.000	0.000	0.058
Mg	0.099	0.114	0.091	0.001
Ca	0.000	0.001	0.000	0.000
Na	0.037	0.034	0.032	0.001
K	0.600	0.595	0.546	0.001
Cations	6.773	6.750	6.720	1.999

*Calculated based on 11 oxygen per formula unit for Muscovite and 3 oxygen per formula unit for Ilmenite, Fe³⁺ from stoichiometry

thickness exhibiting magmatic oscillatory zonation (Fig. 8 a-b). Some zircon cores are homogeneous (Fig. 8a; grain 3,6,10,12) while others show convolute zonation (Fig. 8a;

Fig. 5 a Zr abundance in WGC rocks compared with Zr saturations contours computed for temperature 550–750 °C from empirical formulations (Grevasoni et al. 2016). The Zr content and G values of studied samples reflect Zr saturation of WGC between temperature 550–750 °C. **b** TiO₂–MgO–FeO tripartite plot for WGC biotites (Nachit et al. 2008)



grain 2,5,7–8). Xenocrystic cores are preserved in some zircon grains that exhibit complex zonation and are characterized by resorbed grain boundaries (Fig. 8b, grain 13–16). Most of the zircons lack any metamorphic growth; however, the effects of recrystallization and metamictization are observed in some grains (Fig. 8a, grain 7,8). The U and Th concentrations range from 219 to 1901 ppm and 50 ppm – 462 ppm, respectively, with an average Th/U ratio of 0.3.

The probability density function plot shows two peak ages obtained from the U–Pb ages from the core and rim of the analyzed zircon grains (Fig. 9a). The weighted average ages calculated using Isoplot 4.1 (Ludwig 2012) are (a) 2418 ± 140 Ma (MSWD = 0.061, *n* = 7), and (b) 1846 ± 88 Ma (MSWD = 0.094, *n* = 16). The older peak is at 2418 ± 140 Ma and retrieved from the xenocrystic cores that are possibly derived from an old crustal component. The younger peak is obtained at 1846 ± 88 Ma and retrieved from zircon rims showing magmatic zonation. In a U–Pb Concordia diagram, out of seven spots, a combination of four spots analysis obtained from the zircon cores yield s an upper intercept age of 2487 ± 20 Ma (MSWD = 2.0; concordance percentage > 70%, Fig. 9c). The ages obtained from zircon rims provide an upper intercept age of 1873 ± 15 Ma (MSWD = 2.1; concordance percentage > 70%, Fig. 9d).

Sample WG-86A

A total of 18 spots were analyzed from 15 zircon grains separated from sample WG-86A. The grains are euhedral to subhedral in shape. The size varies between 110 to 220 μm, and the aspect ratio ranges from 2:1 (stubby grains) to 4:1 (elongated grains). The CL imaging reveals that most of the grains display oscillatory zoned rims around distinct cores, reflecting the varying amount of Th and U incorporated during magmatic growth (Fig. 8c). Some zircon cores are homogeneous (Fig. 8c; grain 7,8,9), while others show convolute zonation (Fig. 8c; grain 3,6,11–14). A few zircon grains contain fluid or mineral inclusions (Fig. 8c; grain 1,2,8), suggesting preservation of the primary magmatic character. Some of

Fig. 7 **a** The results of P - T pseudosection analysis using average Jutogh metapelite chemical composition (molar TiO_2 : 0.60, Na_2O : 1.21, CaO : 1.08, K_2O : 2.80, FeO : 4.73, MgO : 3.40, Al_2O_3 : 10.06, H_2O : 1.86, SiO_2 saturated) for sample WG-49; **b-d** The modal abundances of biotite-mica, melt-garnet, and plagioclase, respectively; **e-f** The modeled chemical parameters for silicate melts. A grey-filled box in e marks the suggested P - T condition for melting

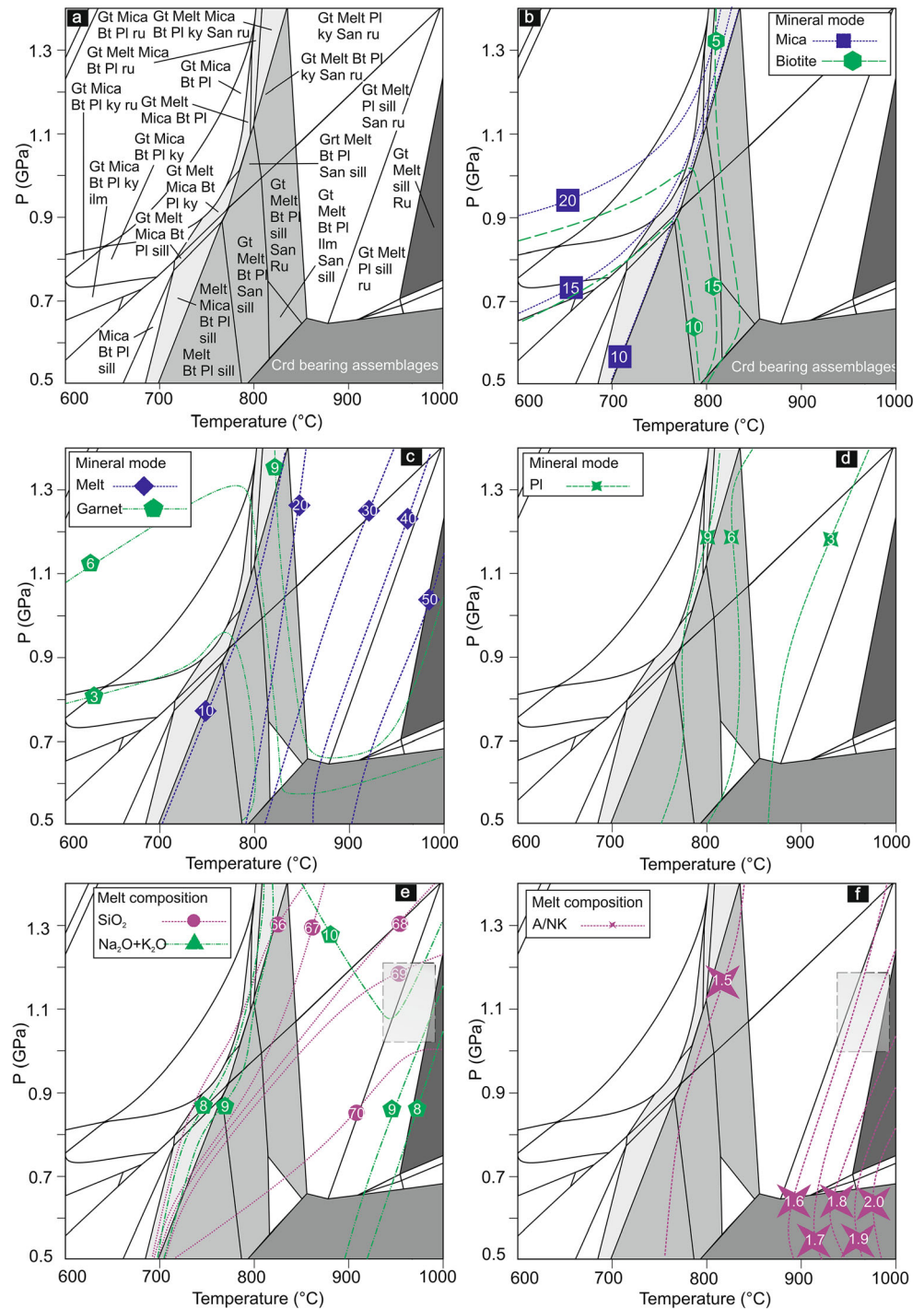


(Fig. 10b, c) after Pearce et al. (1984). Also, the TiO_2 - Al_2O_3 and Y-Zr content of studied samples imply an arc-related origin (Müller et al. 1992, Fig. 10d, e). In addition to the geochemical signatures, the Ti saturation in magmatic zircon (Gervasoni et al. 2016) yields a temperature ~ 600 °C for crystallization temperature for WGC rocks. The temperature estimates from WGC are consistent with the magmatic temperature of S-type granites reported from other parts of the Himalayas (Kohn et al. 2010).

Zircon geochronology

Morphological features, internal zonation, as observed in the CL images, and Th-U content of the analyzed zircon grains imply magmatic origin (Corfu et al. 2003). Also, the presence of fluid and mineral inclusions suggests the perseverance of pristine magmatic character. The upper intercept ages, 1873 ± 15 Ma obtained from the zircon margins of WG-49B, and 1867.7 ± 6.2 Ma obtained from zircons of WG 86A,

Table 6 Zircon U-Pb data (SHRIMP results) for granite (WG-49B) from Wangtu Gneissic Complex

Spot No.	$^{206}\text{Pb}_c$ (%)	U (ppm)	Th (ppm)	Th/ ^{238}U	$^{207}\text{Pb}^*/^{206}\text{Pb}^*$ ($\pm\%$)	$^{207}\text{Pb}^*/^{235}\text{U}$ ($\pm\%$)	$^{206}\text{Pb}^*/^{238}\text{U}$ ($\pm\%$)	Rho	$^{206}\text{Pb}^*/^{238}\text{U}$ Age (Ma)	$^{207}\text{Pb}^*/^{206}\text{Pb}^*$ Age (Ma)	C** (%)						
1.1	0.03	307	56	0.18	3.57	1.24	0.11462	0.59	0.90	4.43	1.4	0.280	1.24	0.90	1593 \pm 17	1874 \pm 11	85
2.1	0.03	458	187	0.41	3.25	0.66	0.11419	0.46	0.82	4.84	0.8	0.307	0.66	0.82	1728 \pm 10	1867 \pm 8	93
3.1	0.00	216	185	0.86	2.24	0.80	0.16215	0.48	0.86	9.97	0.9	0.446	0.80	0.86	2378 \pm 16	2478 \pm 8	96
3.2	0.05	1901	251	0.13	9.29	0.76	0.11086	0.73	0.72	1.65	1.1	0.108	0.76	0.72	659 \pm 5	1814 \pm 13	36
4.1	0.27	1303	44	0.03	5.44	0.69	0.11412	0.44	0.85	2.89	0.8	0.184	0.69	0.85	1088 \pm 7	1866 \pm 8	58
5.1	0.03	276	69	0.25	2.73	0.75	0.15668	0.46	0.85	7.92	0.9	0.367	0.75	0.85	2014 \pm 13	2420 \pm 8	83
5.2	0.08	1316	297	0.23	7.15	0.78	0.12396	0.42	0.88	2.39	0.9	0.140	0.78	0.88	844 \pm 6	2014 \pm 7	42
6.2	0.04	295	200	0.68	2.60	1.03	0.15368	0.45	0.92	8.16	1.1	0.385	1.03	0.92	2101 \pm 18	2387 \pm 8	88
7.1	0.08	631	58	0.09	4.40	1.07	0.11386	0.51	0.90	3.57	1.2	0.227	1.07	0.90	1321 \pm 13	1862 \pm 9	71
8.1	0.05	1404	175	0.12	9.81	0.78	0.10752	0.48	0.85	1.51	0.9	0.102	0.78	0.85	626 \pm 5	1758 \pm 9	36
9.1	0.05	404	175	0.43	3.54	0.68	0.11279	0.52	0.80	4.40	0.9	0.283	0.68	0.80	1605 \pm 10	1845 \pm 9	87
10.1	0.12	251	143	0.57	3.03	1.12	0.15683	0.55	0.90	7.14	1.2	0.330	1.12	0.90	1839 \pm 18	2422 \pm 9	76
10.2	0.05	1646	162	0.10	10.25	1.20	0.10637	0.47	0.93	1.43	1.3	0.098	1.20	0.93	600 \pm 7	1738 \pm 9	35
11.1	0.01	1234	462	0.37	3.76	1.02	0.15006	0.44	0.92	5.51	1.1	0.266	1.02	0.92	1521 \pm 14	2347 \pm 8	65
11.2	0.03	701	128	0.18	3.49	0.62	0.11534	0.37	0.86	4.56	0.7	0.287	0.62	0.86	1624 \pm 9	1885 \pm 7	86
12.1	--	597	176	0.30	3.14	0.64	0.11476	0.40	0.84	5.04	0.8	0.319	0.64	0.84	1783 \pm 10	1876 \pm 7	95
13.1	0.02	790	154	0.20	3.96	0.61	0.11410	0.39	0.84	3.97	0.7	0.252	0.61	0.84	1451 \pm 8	1866 \pm 7	78
14.1	0.02	1113	217	0.19	4.53	0.75	0.15316	0.81	0.68	4.66	1.1	0.221	0.75	0.68	1286 \pm 9	2382 \pm 14	54
15.1	--	443	183	0.41	2.49	1.05	0.16032	0.36	0.94	8.89	1.1	0.402	1.05	0.94	2179 \pm 19	2459 \pm 6	89
16.1	0.05	138	48	0.35	2.99	1.49	0.11487	0.84	0.87	5.30	1.7	0.335	1.49	0.87	1862 \pm 24	1878 \pm 15	99
16.2	0.03	299	84	0.28	3.18	0.74	0.11365	0.57	0.79	4.93	0.9	0.315	0.74	0.79	1764 \pm 11	1859 \pm 10	95

Errors are 1-sigma; Pb_c and Pb^* indicate the common and radiogenic portions, respectively; common Pb corrected using measured ^{204}Pb . C**-. Degree of concordancy (i.e., quotient of the ^{204}Pb -corrected $^{206}\text{Pb}/^{238}\text{U}$ and $^{207}\text{Pb}/^{206}\text{Pb}$ ages multiplied by 100)

Table 7 Zircon U-Pb data (SHRIMP results) for granite (WG-86A) from Wangtu Gneissic Complex

Spot No.	$^{206}\text{Pb}_c$ (%)	U (ppm)	Th (ppm)	Th/U	$^{238}\text{U}/^{206}\text{Pb}^*$ ($\pm\%$)	$^{207}\text{Pb}^*/^{206}\text{Pb}^*$ ($\pm\%$)	Rho ($\pm\%$)	$^{207}\text{Pb}^*/^{235}\text{U}$ ($\pm\%$)	$^{206}\text{Pb}^*/^{238}\text{U}$ ($\pm\%$)	Rho ($\pm\%$)	$^{206}\text{Pb}/^{238}\text{U}$ Age (Ma)	$^{207}\text{Pb}/^{206}\text{Pb}$ Age (Ma)	C^{**} (%)	
1.1	0.07	619	86	0.14	3.84	0.652 0.114	0.810 0.63	4.09	1.04	0.260	0.652 0.63	1491 \pm 9	1865 \pm 15	80
1.2	0.03	513	128	0.25	3.14	0.655 0.114	0.872 0.60	5.01	1.09	0.318	0.655 0.60	1781 \pm 10	1868 \pm 16	95
2.1	0.17	138	48	0.35	3.35	0.934 0.115	0.941 0.70	4.74	1.33	0.299	0.934 0.70	1686 \pm 14	1881 \pm 17	90
2.2	0.04	827	241	0.29	4.30	0.608 0.114	0.732 0.64	3.65	0.95	0.233	0.608 0.64	1349 \pm 7	1862 \pm 13	72
3.1	0.02	944	261	0.28	6.07	1.027 0.113	0.454 0.91	2.56	1.12	0.165	1.027 0.91	983 \pm 9	1845 \pm 8	53
4.1	0.06	868	37	0.04	4.23	0.935 0.114	0.714 0.79	3.73	1.18	0.236	0.935 0.79	1368 \pm 12	1872 \pm 13	73
4.2	0.02	867	266	0.31	4.15	0.604 0.114	0.816 0.59	3.78	1.02	0.241	0.604 0.59	1391 \pm 8	1863 \pm 15	75
5.1	--	405	132	0.33	3.04	0.700 0.114	0.506 0.81	5.15	0.86	0.329	0.700 0.81	1831 \pm 11	1858 \pm 9	99
6.1	0.03	831	252	0.30	4.97	0.620 0.114	0.721 0.65	3.16	0.95	0.201	0.620 0.65	1183 \pm 7	1862 \pm 13	63
7.1	--	565	266	0.47	3.18	0.648 0.115	0.420 0.84	5.00	0.77	0.315	0.648 0.84	1764 \pm 10	1883 \pm 8	94
8.1	0.06	657	137	0.21	3.71	0.627 0.113	0.431 0.82	4.19	0.76	0.269	0.627 0.82	1537 \pm 9	1848 \pm 8	83
9.1	0.04	594	267	0.45	3.23	0.635 0.115	0.405 0.84	4.90	0.75	0.309	0.635 0.84	1737 \pm 10	1878 \pm 7	92
10.1	0.03	357	123	0.34	3.17	0.702 0.114	0.525 0.80	4.96	0.88	0.316	0.702 0.80	1770 \pm 11	1862 \pm 9	95
11.1	--	682	197	0.29	3.50	0.625 0.114	0.396 0.84	4.51	0.74	0.286	0.625 0.84	1621 \pm 9	1869 \pm 7	87
12.1	0.00	454	137	0.30	3.20	0.988 0.113	0.473 0.90	4.87	1.10	0.312	0.988 0.90	1752 \pm 15	1850 \pm 9	95
13.1	0.06	821	232	0.28	4.95	0.608 0.114	0.463 0.80	3.18	0.76	0.202	0.608 0.80	1186 \pm 7	1865 \pm 8	64
14.1	0.05	664	194	0.29	3.62	0.630 0.113	0.432 0.82	4.32	0.76	0.276	0.630 0.82	1572 \pm 9	1855 \pm 8	85
15.1	0.03	682	191	0.28	3.53	0.631 0.114	0.427 0.83	4.44	0.76	0.283	0.631 0.83	1609 \pm 9	1857 \pm 8	87

Errors are 1-sigma; Pb_c and Pb^* indicate the common and radiogenic portions, respectively; common Pb corrected using measured ^{204}Pb . C^{**} -. Degree of concordancy (i.e., quotient of the ^{204}Pb -corrected $^{206}\text{Pb}/^{238}\text{U}$ and $^{207}\text{Pb}/^{206}\text{Pb}$ ages multiplied by 100)

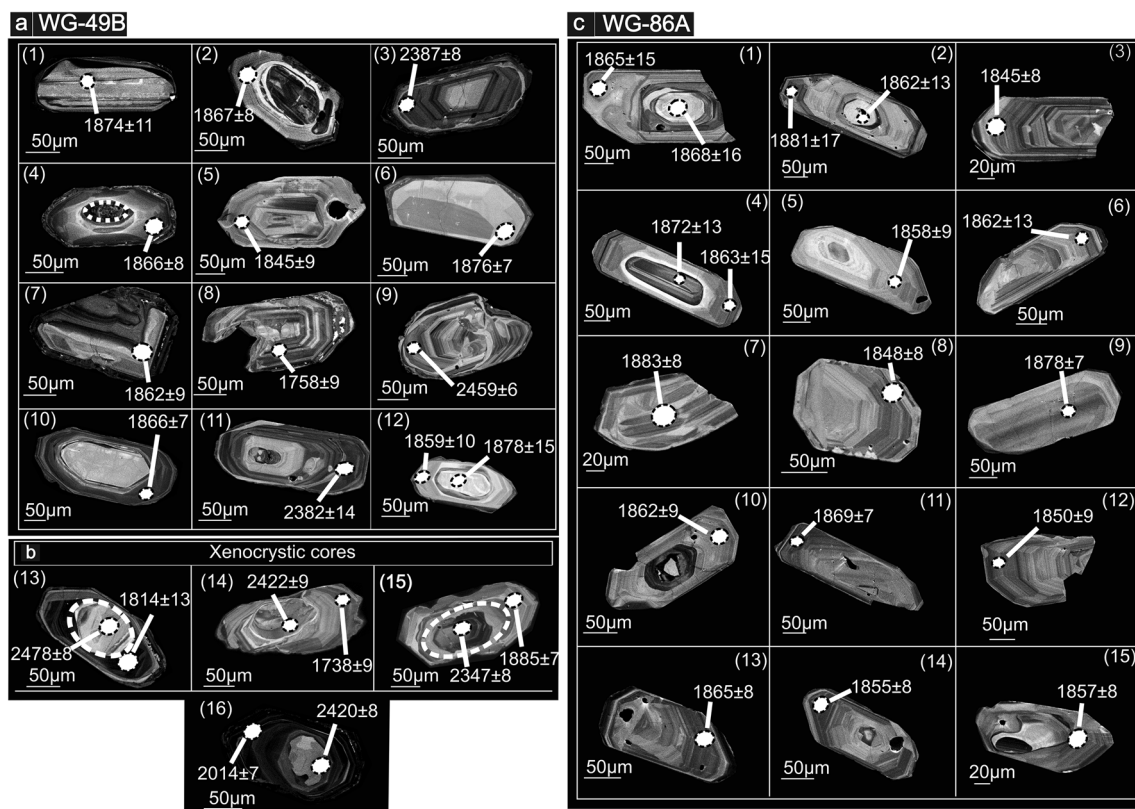


Fig. 8 a–b CL images of representative zircon grains from WG-49B and WG-86A. c CL images of representative zircon grains from WG-49B and WG-86A. The Pb–Pb spot ages are shown for each grain.

respectively, is similar and overlap with the U–Pb ages obtained from Kumaon Himalaya (Phukon et al. 2018); Uttarakhand Himalaya (Mukherjee et al. 2019); Nepal Himalaya (Kohn et al. 2010); Bhutan and Arunachal Himalaya (Pathak and Kumar 2019). The older ages obtained from the zircon core with an upper intercept of 2487 ± 20 Ma in WG 49B reveal the contribution of ~ 2500 Ma crustal materials either from the adjacent Bundelkhand craton (Saha et al. 2016; Nasipuri et al. 2019 and references therein) and Aravalli craton (Kaur et al. 2013). The convolute zonation is preserved as ~ 2500 Ma core in zircon grains (Fig. 9a), imply high-temperature metamorphism in the adjoining Archean cratons (c.f. Harley et al. 2007). The results of geochemistry and geochronology from the present study, when compared with the geochemistry of ~ 1800 Ma LH granites along the Himalayas, point towards the existence of a volcanic arc, temporally similar to those suggested from different segments of LH.

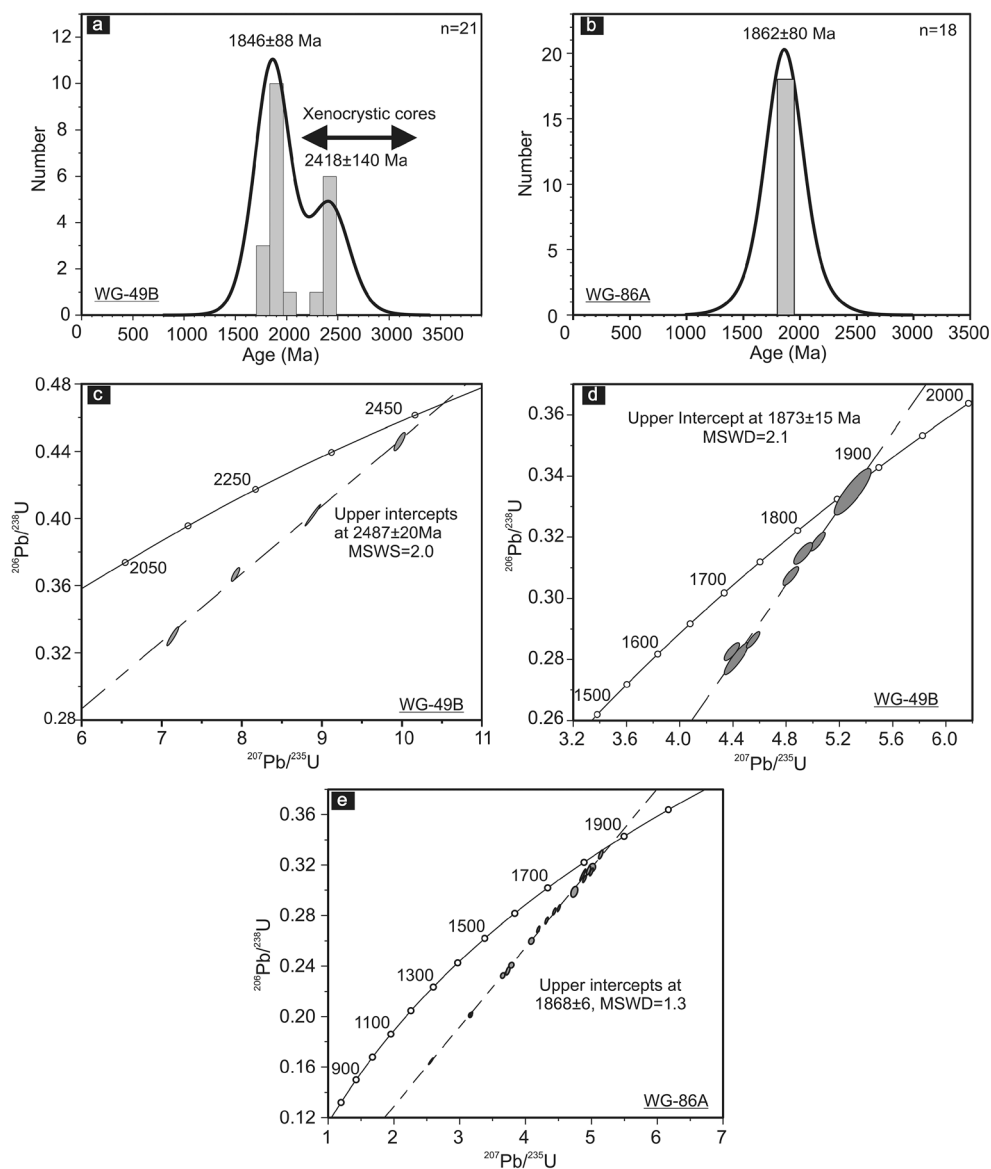
Possible *P–T* conditions

In the last three decades, several researchers, e.g., Le Breton and Thompson (1988); Conrad et al. (1988); Vielzeuf and Holloway (1988); Patiño Douce and Johnston (1991); Vielzeuf and Montel (1994); Carrington and Harley (1995); Gardien et al. (1995); Montel and

Vielzeuf (1997); Patiño Douce and Harris (1998); Anenburg and Katzir (2013); and Dyck et al. (2020) have studied the significance of muscovite and biotite melting in metapelites and other mica-rich rocks for the origin of magma parental to S-type granites.

A compilation of available experimental data implies that muscovite reacts with quartz to produce sillimanite, K-feldspar, and silicate melt in dry rocks (Patiño Douce and Harris 1998; Pickering and Johnston 1998). The H_2O present muscovite melting produces melt and sillimanite (without K-feldspar) as a peritectic phase (Patiño Douce and Harris 1998). Similarly, the fluid absent, biotite melting in metapelites, produces K-feldspar-garnet-cordierite along with silicate melt (Le Breton and Thompson 1988; Patiño Douce and Harris 1998). The phase stability information from melting experiments indicates that muscovite stability in metapelite depends on the amount of free H_2O present in the rock, as dehydration melting of mica begins at $750\text{--}800$ °C, in contrast to the H_2O saturated melting that begins at relatively lower temperature $\sim < 730$ °C– 750 °C (Patiño Douce and Harris 1998; Pickering and Johnston 1998). Biotite is relatively stable at a higher temperature compared to muscovite and begins melting at temperature > 812 °C to produce silicate melt and restite garnet (Pickering and Johnston 1998; Gardien et al. 2000).

Fig. 9 **a–b** Probability density function plots for sample WG-49B and WG-86A. The weighted average ages for statistically separable groups are also given. **c–e** U–Pb Concordia plots for samples WG-49 and WG-86, respectively. Ellipses indicate 1σ uncertainty, which is smaller than the symbols used in the main plot. MSWD – mean square weighted deviation



Several researchers, e.g., White et al. (2001, 2014); Brown (2007a); Holland and Powell (2011); Korhonen et al. (2013b, 2015) have modeled mica and biotite melting in TiNCKFMASH chemical systems to understand the interplay between subsolidus stability of hydrous minerals, its dehydration melting mechanisms and volume of magma production. The modeled phase relations for the Jutogh metasediments (Fig. 7a) are comparable with the P – T pseudosection constructed from average metapelite composition (Harris et al. 2000; Tinkham et al. 2001; Brown 2007b; White et al. 2007; Korhonen et al. 2013a, 2015; Fumes et al. 2019). Among several similar phase relations between the Jutogh metasediments and ideal metapelite phase topology, the most significant is the appearance of silicate melt at ~ 750 – 800 °C, and finally complete exhaustion of hydrous minerals and stability of garnet, sillimanite, rutile along with silicate melt at temperature > 850 °C. The modeled abundances of muscovite

reveal that muscovite begin melting at temperature ~ 700 °C under H_2O saturated condition and is completely exhausted at temperature 800 °C, between pressure 0.5 – 1.4 GPa. Biotite is relatively stable at a higher temperature and is completely destabilized at a temperature ~ 850 °C—the modeled abundances of melt and garnet increase with an increase in temperature in the P – T pseudosection. The steep positive slope of the ‘melt-in’ line also implies that magma production is principally due to mica and biotite melting due to an increase in temperature and pressure along a prograde segment of a P – T path.

The SiO_2 and $\text{Na}_2\text{O} + \text{K}_2\text{O}$ contents of silicate melts increase with temperature. The compositional isopleths for melt and the modal abundances of biotite and muscovite when compared together also imply destabilization of muscovite and biotite, leading to SiO_2 and $\text{Na}_2\text{O} + \text{K}_2\text{O}$ enrichment in the modeled silicate melt composition with an increase in temperature. The intersection of modelled isopleths having

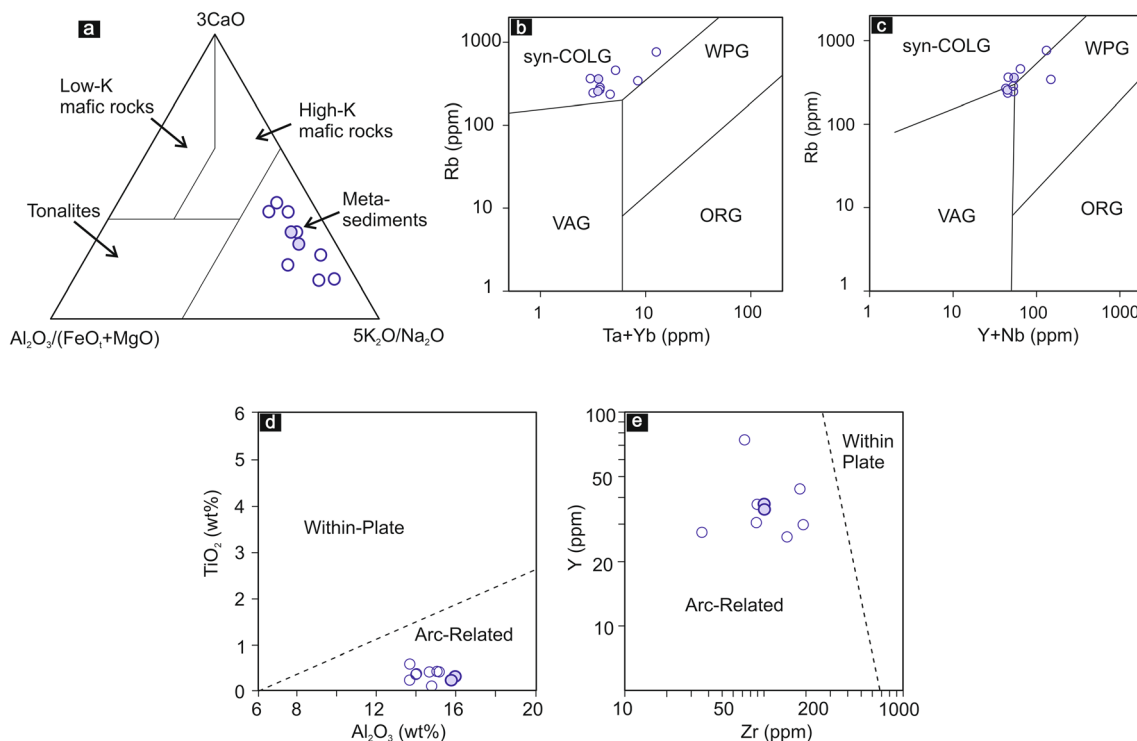


Fig. 10 **a** $\text{Al}_2\text{O}_3/(\text{FeO} + \text{MgO}) - 3 \times \text{CaO} - 5 \times (\text{K}_2\text{O}/\text{Na}_2\text{O})$ ternary plot for studied samples. In the triangular plot, the different source fields are after Laurent et al. (2014). **b** Rb – (Yb + Ta) and **c** Rb – (Y + Nb) plot for the studied samples. The different tectonic settings are adapted from Pearce et al. (1984). Abbreviations: syn-COLG – syn-collisional granite,

WPG – within plate granite, ORG – ocean ridge granite, VAG – volcanic arc granites. **d-e** $\text{TiO}_2 - \text{Al}_2\text{O}_3$ and Y – Zr plots of the studied samples to discriminate between “within plate” and “arc-related” related tectonic settings (Muller et al. 2010)

values similar to the averaged WGC, i.e., SiO_2 68–70 wt% and $(\text{Na}_2\text{O} + \text{K}_2\text{O}) \sim 8.5$ wt% intersect at 850–900 °C and 1.2–1.3 GPa. The modeled P - T conditions correspond to a crustal depth of ~45 km with a geothermal gradient >750 °C/GPa (Brown 2014).

The P - T modeling also predicts 60–70 vol% melt, 5–6 vol% garnet, and 3–4 vol% rutile in the P - T window defined intersection of modeled chemical parameters as the anticipated melt volume is higher than the limits of the melt percolation threshold for granitic magma (~20–25% of melt, Vigneresse et al. 1996), the melt thus generated by melting of biotite and muscovite can leave the system and ascent upwards by leaving the garnet and rutile residue in the lower crustal levels.

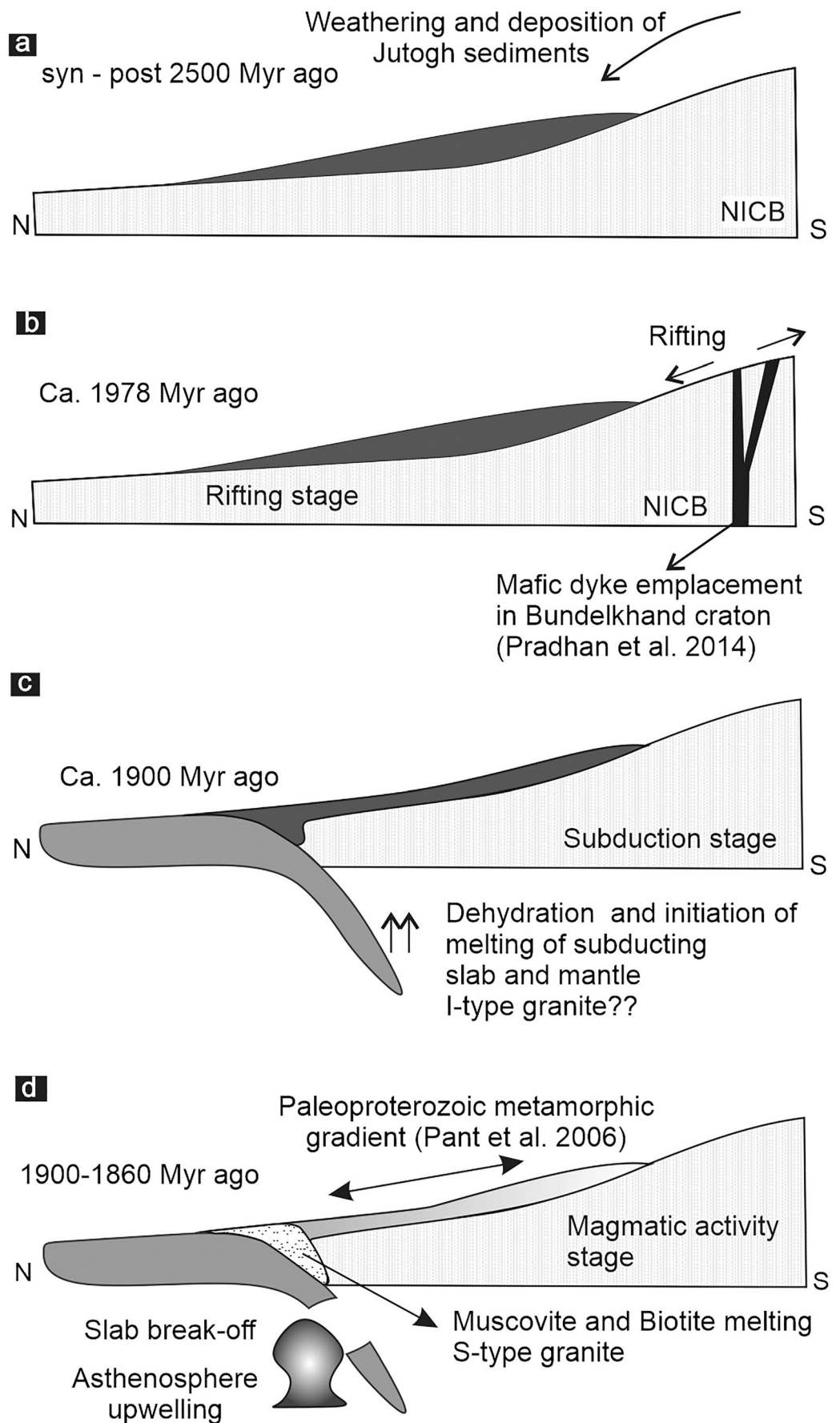
Tectonic model

A correlation of the geochemistry and emplacement ages of LH granites with the paleogeographical maps of Columbia implies two possible tectonic settings of the northern margin of the Indian peninsula. First of all, the anorogenic A-type granite emplacement in parts of Rajasthan (Pandit and Khatatneh 1998; Kaur et al. 2011b, 2017) and lesser Himalaya (Singh and Jain 2003; Saha 2013; Larson et al. 2019; Singh 2020) in 2100–1800 Ma suggested, the northern margin of Indian Peninsula is probably a passive margin, as indicated in the

Columbia models after Rogers and Santosh (2002) and Zhao et al. (2011). On the contrary, recent reports of 2100–1800 Ma S-type granites from the LH rocks (Kohn et al. 2010; Phukon et al. 2018; Pathak and Kumar 2019) imply the existence of a volcanic arc and subduction zone beneath the NICB, in agreement with the paleogeographic models after Hou et al. (2008). In the following sections, P - T conditions for granite emplacement and melt generations *m* and projected geothermal gradients are combined with geochronological data that provide valuable insights for the tectonic characterization of the northern margin of the Indian plates.

Based on the geochemical, geochronological results, and P - T pseudosection modeling, we suggest a tectonic scenario where sediments similar in composition with Jutogh metasediments were deposited in a paleo-ocean basin at the northern boundary of the NICB. The ~2500 Ma zircon cores in WGC suggest that sediments were probably derived from weathering of ~2500 Ma K-feldspar granites from the adjoining NICB, comprising the Archean Aravalli and Bundelkhand craton (Fig. 11a). The initiation of extensional tectonics in the NICB is marked by emplacement of mafic dykes at 1978 ± 8 Ma in Mahoba, Bundelkhand craton (Pradhan et al. 2012). French et al. (2008), Söderlund et al. (2019) reported 2370–1790 Ma extensional tectonics and mafic dyke emplacement from the Bastar and the Dharwar craton. We suggest that the

Fig. 11 Cartoon showing the possible tectonic scenario on NICB (not to scale). **a** Configuration of the North Indian Continental Block (NICB) syn-post 2500 Myr ago. Chemical weathering of NICB and its subsequent deposition led to the formation of Jutogh metasedimentary sequences; **b** At 1978 Myr ago rifting and mafic dyke emplacement in the Bundelkhand craton. The rifting can provide additional horizontal force for the northward movement of parts of NICB; **c** Initiation of subduction below NICB at ~1900 Myr ago; **d** Slab breakoff and asthenosphere upwelling at the base of NICB to initiate mica and biotite melting and formation of S-type granite between 1900 and 1860 Myr ago



rifting and mafic dyke emplacement in the NICB and SICB should have provided the necessary horizontal force for the north-ward movement by initiating a subduction zone trench-volcanic arc system at the northern margin of NICB (Fig. 11b). As the subduction process continues, the melting of the subducting slab leads to I type magma formation and its emplacement at the base of NICB (Fig. 11c). The geochemistry and modeled P - T conditions for magma generation, i.e., temperature ~ 900 °C, pressure 1.1–1.2 GPa, correspond to a geothermal gradient of 1000 °C/GPa indicative of a magma ponding and melting of crustal materials. The ongoing subduction and melting of the oceanic crust will lead to slab breakoff and asthenosphere upwelling that can provide additional heat for the melting of the Jutogh metasediments for the genesis of the WGC (Fig. 11d). Pant et al. (2006) document high-temperature contact metamorphism from Jutogh metasediments, probably due to the emplacement of 1800 Ma granites. Therefore, this article's suggested tectonic model also explains Paleoproterozoic contact metamorphism in the metasedimentary rocks adjacent to the WGC. Subsequently, extensive asthenosphere melting in the back-arc region may cause rifting and emplacement of A-type granite (Singh et al. 2009).

Conclusions

The results of this study imply that a majority of the WGC rocks resemble peraluminous S-type granite. The results of Ti in Zircon thermometry and P - T pseudosection analysis constrain temperature ~ 600 °C and pressure 0.9–1.1 GPa as magmatic crystallization conditions. The predominant U-Pb zircon ages from WGC imply magmatism during 1867–1873, Ma. Accordingly, the ~ 2500 Ma zircon cores reveal the contribution of older crustal materials in the protoliths parental to WGC magma. Finally, the phase-equilibria modeling implies that 60–70% melting of the metasediments similar in composition to the present-day Jutogh metasedimentary sequences at temperature ~ 850 °C and pressure 1.1–1.2 GPa can produce magma similar in composition to WGC. The tectonic setting and magmatic events in the LH rocks from Himachal Himalaya can be correlated with the 1900–1800 Ma subduction driven global magmatism related to the Columbia assembly.

Supplementary Information The online version contains supplementary material available at <https://doi.org/10.1007/s00710-021-00738-y>.

Acknowledgments The research work is part of Hifzurrahman's Ph.D. thesis under the University Grants Commission, India – Maulana Azad National Fellowship Scheme. Hifzurrahman acknowledges the help of Yogesh Kumar in the initial fieldwork. We thank Virendra M. Tiwari, Director of the National Geophysical Research Institute (NGRI), and Ram Mohan for geochemical analysis. We gratefully acknowledge the

comments and suggestions of two anonymous reviewers, Tamer A. Alam, and journal editors Qiuli Li and Lutz Nasdala. P.N. acknowledges financial support from the Ministry of Earth Sciences, India Project MoES/P. O/(GEO)/101(3)/2017 for supporting fieldwork, petrography, and geochemical analysis. Funding for U-Pb SHRIMP analysis was provided by Siva Umopathy, Director of the Indian Institute of Science Education and Research, Bhopal.

References

- Ahmad T (2008) Precambrian mafic magmatism in the Himalayan mountain range. *J Geol Soc India* 72:85–92
- Ahmad T, Mukherjee P, Trivedi J (1999) Geochemistry of Precambrian mafic magmatic rock of the Western Himalaya, India: petrogenetic and tectonic implications. *Chem Geol* 160:103–119
- Ahmad T, Harris N, Bickle M, Chapman H, Bunbury J, Prince C (2000) Isotopic constraints on the structural relationships between the lesser Himalayan series and the high Himalayan crystalline series, Garhwal Himalaya. *Bull Geol Soc Am* 112:467–477
- Anenburg M, Katzir Y (2013) Muscovite dehydration melting in Si-rich metapelites: microstructural evidence from trondhjemitic migmatites, Roded, southern Israel. *Miner Petrol* 108:137–152
- Basu Sarbadhikari A, Bhowmik SK (2008) Constraining the metamorphic evolution of a cryptic hot Mesoproterozoic orogen in the central Indian tectonic zone, using P-T pseudosection modelling of mafic intrusions and host reworked granulites. *Precambrian Res* 162:128–149
- Bhandari A, Chandra Pant N, Bhowmik SK, Goswami S (2011) ~ 1.6 Ga ultrahigh-temperature granulite metamorphism in the central Indian tectonic zone: insights from metamorphic reaction history, geothermobarometry and monazite chemical ages. *Geol J* 46: 198–216
- Bhat MI, Le Fort P (1992) Sm-Nd age and petrogenesis of Rampur metavolcanic rocks, NW Himalayas: late Archaean relics in the Himalayan belt. *Precambrian Res* 56:191–210
- Bhat MI, Claesson S, Dubey AK, Pande K (1998) Sm-Nd age of the Garhwal-Bhowali volcanics, western Himalayas: vestiges of the late Archaean Rampur flood basalt province of the northern Indian Craton. *Precambrian Res* 87:217–231
- Bhowmik SK (2019) The current status of orogenesis in the central Indian tectonic zone: a view from its southern margin. *Geol J* 54: 2912–2934
- Bhowmik SK, Saha L, Dasgupta S, Fukuoka M (2009) Metamorphic phase relations in orthopyroxene-bearing granitoids: implication for high-pressure metamorphism and prograde melting in the continental crust. *J Metamorph Geol* 27:295–315
- Bhowmik SK, Wilde SA, Bhandari A, Pal T, Pant NC (2012) Growth of the greater Indian landmass and its assembly in Rodinia: Geochronological evidence from the central Indian tectonic zone. *Gondwana Res* 22:54–724
- Briqueu L, Bougault H, Joron JL et al (1984) Quantification of Nb, Ta, Ti and V anomalies in magmas associated with subduction 'zones' petrogenetic implications Louis Briqueu 1, H. Bougault 2 and Jean Louis Joron 3. *Earth Planet Sci* 68:297–308
- Brookfield ME (1993) The Himalayan passive margin from Precambrian to cretaceous times. *Sediment Geol* 84:1–35
- Brown M (2007a) Metamorphic conditions in orogenic belts: a record of secular change. *Int. Geol Rev* 3:193–234
- Brown M (2007b) Metamorphism, plate tectonics, and the supercontinent cycle. *Earth Sci Front* 14:1–18
- Brown M (2008) Characteristic thermal regimes of plate tectonics and their metamorphic imprint throughout earth history: when did earth

- first adopt a plate tectonics mode of behavior *Spec Pap Geol Soc Am* 440:97–128
- Carrington DP, Harley SL (1995) Partial melting and phase relations in high-grade metapelites: an experimental petrogenetic grid in the KFMASH system. *Contrib to Mineral Petrol* 120:270–291
- Chakrabarti BK (2016) *Geology of the Himalayan Belt*. Elsevier
- Chambers JA, Argles TW, Horstwood MSA et al (2008) Tectonic implications of Palaeoproterozoic anatexis and Late Miocene metamorphism in the lesser Himalayan sequence, Sutlej Valley, NW India. *J Geol Soc Lond* 165:725–737
- Chambers J, Caddick M, Argles T, Horstwood M, Sherlock S, Harris N, Parrish R, Ahmad T (2009) Empirical constraints on extrusion mechanisms from the upper margin of an exhumed high-grade orogenic core, Sutlej valley, NW India. *Tectonophysics* 477:77–92
- Chappell B, White A (2001) Two contrasting granite types: 25 years later. *Aust J Earth Sci* 48:489–499
- Chatterjee N, Bhattacharji S (2001) Petrology, geochemistry and tectonic settings of the mafic dikes and sills associated with the evolution of the Proterozoic Cuddapah Basin of South India. *Proc Indian Acad Sci Earth Planet Sci* 110:433–453
- Chatterjee N, Ghose NC (2011) Extensive early Neoproterozoic high-grade metamorphism in north Chotanagpur gneissic complex of the central Indian tectonic zone. *Gondwana Res* 20:362–379
- Coggon R, Holland TJB (2002) Mixing properties of phengitic micas and revised garnet-phengite thermobarometers. *J Metamorph Geol* 20:683–696
- Collins AS, Pisarevsky SA (2005) Amalgamating eastern Gondwana: the evolution of the Circum-Indian Orogens. *Earth-Science Rev* 71:229–270
- Connolly JAD (2009) The geodynamic equation of state: what and how. *Geochemistry, Geophys Geosystems* 10:1–19
- Conrad W, Nicholls I, Wall V (1988) Water-saturated and -undersaturated melting of Metaluminous and Peraluminous crustal compositions at 10 kb: evidence for the origin of silicic magmas in the Taupo volcanic zone, New Zealand, and other occurrences. *J Petrol* 29:765–803
- Corfu F, Hanchar JM, Hoskin PW, Kinny P (2003) Atlas of zircon textures. *Rev Mineral Geochem* 53:469–500 Dalziel IWD, Mosher S, Gahagan LM (2000) Laurentia-Kalahari collision and the assembly of Rodinia. *J Geol* 108:499–513
- Dalziel I, Mosher S, Gahagan L (2000) Laurentia-kalahari collision and the assembly of rodinia. *J Geol* 108(5):499–513
- Deer WAFRS, Howie RA, Zussman J (2013) *An Introduction to the Rock-Forming Minerals*. Mineralogical Society of Great Britain and Ireland
- Dyck B, Waters DJ, St-Onge MR, Searle MP (2020) Muscovite dehydration melting: reaction mechanisms, microstructures, and implications for anatexis. *J Metamorph Geol* 38:29–52
- Evans DAD, Mitchell RN (2011) Assembly and breakup of the core of Paleoproterozoic-Mesoproterozoic supercontinent Nuna. *Geology* 39(5):443–446
- Finger F, Schiller D (2012) Lead contents of S-type granites and their petrogenetic significance. *Contrib Mineral Petrol* 164:747–755
- French J, Heaman L, Chacko T, Srivastava R (2008) 1891–1883 ma southern Bastar–Cuddapah mafic igneous events, India: a newly recognized large igneous province. *Precambrian Res* 160:308–322
- Fumes RA, Luvizotto GL, Moraes R et al (2019) Metamorphic modeling and petrochronology of metapelitic rocks from the Luminarias Nappe, southern Brasilia belt (SE Brazil). *Brazilian J Geol* 49:1–25
- Gansser A (1964) *Geology of the Himalayas*. John Wiley and Sons Ltd
- Gardien V, Thompson AB, Grujic D, Ulmer P (1995) Experimental melting of biotite + plagioclase + quartz ± muscovite assemblages and implications for crustal melting. *J Geophys Res* 100:15581–15591
- Gardien V, Thompson AB, Ulmer P (2000) Melting of Biotite + plagioclase + quartz gneisses: the role of H₂O in the stability of amphibole. *J Petrol* 41:651–656
- Gehrels GE, DeCelles PG, Ojha TP, Upreti BN (2006) Geologic and U-Th-Pb geochronologic evidence for early Paleozoic tectonism in the Kathmandu thrust sheet, Central Nepal Himalaya. *Bull Geol Soc Am* 118:185–198
- Gervasoni F, Klemme S, Rocha-Júnior ERV, Berndt J (2016) Zircon saturation in silicate melts: a new and improved model for aluminous and alkaline melts. *Contrib Mineral Petrol* 171:1–12
- Goode JW, Fanning CM (2016) Mesoarchean and Paleoproterozoic history of the nimrod complex, central Transantarctic Mountains, Antarctica: stratigraphic revisions and relation to the Mawson continent in East Gondwana. *Precambrian Res* 285:242–271
- Goode JW, Fanning CM, Bennett VC (2001) U-Pb evidence of ~1.7 Ga crustal tectonism during the nimrod orogeny in the Transantarctic Mountains, Antarctica: implications for Proterozoic plate reconstructions. *Precambrian Res* 112:261–288
- Harley SL, Nandakumar V (2016) New evidence for Palaeoproterozoic high grade metamorphism in the Trivandrum block, southern India. *Precambrian Res* 280:120–138
- Harley SN, Kelly NM, Moller A (2007) Zircon Behaviour and the Thermal Histories of Mountain Chains. *Elements* 3(1):25–30
- Harris N, Vance D, Ayres M (2000) From sediment to granite: timescales of anatexis in the upper crust. *Chem Geol* 162:155–167
- Harrison TM, Ryerson FJ, Le Fort P et al (1997) A Late Miocene-Pliocene origin for the central Himalayan inverted metamorphism. *Earth Planet Sci Lett* 146:E1–E7
- Henry DJ, Guidotti CV, Thomson JA (2005) The Ti-saturation surface for low-to-medium pressure metapelitic biotites: implications for geothermometry and Ti-substitution mechanisms. *Am Mineral* 90:316–328
- Hoffman P (1988) United plates of America, the birth of a Craton: early Proterozoic assembly and growth of Laurentia. *Annu Rev Earth Planet Sci* 16:543–603
- Hoffman PF (1991) Did the breakout of Laurentia turn Gondwanaland inside-out? *Science* 252:1409–1412
- Holland TJB, Powell R (2001) Calculation of phase relations involving Haplogranitic melts using an internally consistent thermodynamic dataset. *J Petrol* 42:673–683
- Holland TJB, Powell R (2011) An improved and extended internally consistent thermodynamic dataset for phases of petrological interest, involving a new equation of state for solids. *J Metamorph Geol* 29:333–383
- Hou G, Santosh M, Qian X, Lister GS, Li J (2008) Configuration of the late Paleoproterozoic supercontinent Columbia: insights from radiating mafic dyke swarms. *Gondwana Res* 14:395–409
- Irvine TN, Baragar WRA (1971) A guide to the chemical classification of the common volcanic rocks. *Can J Earth Sci* 8:523–548
- Jain AK, Manickavasagam RM (1993) Inverted metamorphism in the intracontinental ductile shear zone during Himalayan collision tectonics. *Geology* 21:407–410
- Kaur P, Chaudhri N, Raczek I et al (2007) Geochemistry, zircon ages and whole-rock Nd isotopic systematics for Palaeoproterozoic A-type granitoids in the northern part of the Delhi belt, Rajasthan, NW India: implications for late Palaeoproterozoic crustal evolution of the Aravalli craton. *Geol Mag* 144:361–378
- Kaur P, Chaudhri N, Raczek I, Kröner A, Hofmann AW (2009) Record of 1.82 Ga Andean-type continental arc magmatism in NE Rajasthan, India: insights from zircon and Sm-Nd ages, combined with Nd-Sr isotope geochemistry. *Gondwana Res* 16:56–71
- Kaur P, Chaudhri N, Raczek I, Kröner A, Hofmann AW, Okrusch M (2011a) Zircon ages of late Palaeoproterozoic (ca. 1.72–1.70 Ga) extension-related granitoids in NE Rajasthan, India: regional and tectonic significance. *Gondwana Res* 19:1040–1053
- Kaur P, Zeh A, Chaudhri N, Gerdes A, Okrusch M (2011b) Archaean to Palaeoproterozoic crustal evolution of the Aravalli mountain range, NW India, and its hinterland: the U-Pb and Hf isotope record of detrital zircon. *Precambrian Res* 187:155–164

- Kaur P, Chaudhri N, Hofmann AW, Raczek I, Okrusch M (2013a) Geochemistry and Sm-Nd geochronology of the metasomatised mafic rocks in the Khetri complex, Rajasthan, NW India: evidence of an early Cryogenian metasomatic event in the northern Aravalli orogen. *J Asian Earth Sci* 62:401–413
- Kaur P, Zeh A, Chaudhri N, Gerdes A, Okrusch M (2013b) Nature of magmatism and sedimentation at a Columbia active margin: insights from combined U-Pb and Lu-Hf isotope data of detrital zircons from NW India. *Gondwana Res* 23:1040–1052
- Kaur P, Chaudhri N, Hofmann AW (2015) New evidence for two sharp replacement fronts during albitization of granitoids from northern Aravalli orogen, Northwest India. *Int Geol Rev* 57:1660–1685
- Kaur P, Zeh A, Chaudhri N, Elias N (2017) Two distinct sources of 1.73–1.70 Ga A-type granites from the northern Aravalli orogen, NW India: constraints from in situ zircon U-Pb ages and Lu-Hf isotopes. *Gondwana Res* 49:164–181
- Kohn MJ, Paul SK, Corrie SL (2010) The lower lesser himalayan sequence: a paleoproterozoic arc on the northern margin of the Indian plate. *Bull Geol Soc Am* 122:323–335
- Korhonen FJ, Brown M, Clark C, Bhattacharya S (2013a) Osumilite-melt interactions in ultrahigh temperature granulites: phase equilibria modelling and implications for the P-T-t evolution of the eastern ghats province, India. *J Metamorph Geol* 31:881–907
- Korhonen FJ, Clark C, Brown M, Bhattacharya S, Taylor R (2013b) How long-lived is ultrahigh temperature (UHT) metamorphism? Constraints from zircon and monazite geochronology in the eastern Ghats orogenic belt, India. *Precambrian Res* 234:322–350
- Korhonen F, Brown M, Clark C, Foden JD, Taylor R (2015) Are granites and granulites consanguineous? *Geology* 43:991–994
- Krishna K, Murthy N, Govil P (2007) Multielement analysis of soils by wavelength-dispersive x-ray fluorescence spectrometry. *Atomic Spectroscopy* 28:202–214
- Larson K, Piercey S, Cottle J (2019) Preservation of a Paleoproterozoic rifted margin in the Himalaya: insight from the Ulleri-Phaplumelung orthogneiss. *Geosci Front* 10:873–883
- Laurent O, Martin H, Moyen JF, Doucelance R (2014) The diversity and evolution of late-Archean granitoids: evidence for the onset of “modern-style” plate tectonics between 3.0 and 2.5 Ga. *Lithos* 205:208–235
- Le Breton N, Thompson AB (1988) Fluid-absent (dehydration) melting of biotite in metapelites in the early stages of crustal anatexis. *Contrib to Mineral Petrol* 99:226–237
- Le Fort P (1975) Himalayas: the collided range. Present knowledge of the continental arc. *Am J Sci* 275:1–44
- Liu X, Zhao Y, Chen H, Song B (2017) New zircon U–Pb and Hf–Nd isotopic constraints on the timing of magmatism, sedimentation and metamorphism in the northern Prince Charles mountains, East Antarctica. *Precambrian Res* 299:15–33
- Ludwig KR (2009) Isoplot A Geochronological Tool Kit for Microsoft Excell Berkeley Geochronol Cent Spec Publ No 4:76
- Ludwig KR (2012) Isoplot 3.75. A Geochronological toolkit for Microsoft excel. Berkeley Geochronol Cent Spec Publ No 5:1–75
- Mandal B, Sen MK, Rao VV (2013) New seismic images of the Central Indian Suture Zone and their tectonic implications. *Tectonics* 32:908–921
- Mandal S, Robinson DM, Kohn MJ, Khanal S, Das O, Bose S (2016) Zircon U-Pb ages and Hf isotopes of the Askot klippe, Kumaun, Northwest India: implications for Paleoproterozoic tectonics, basin evolution and associated metallogeny of the northern Indian cratonic margin. *Tectonics* 35:965–982
- McDonough, Sun (1995) The composition of the earth. *Chem Geol* 67:1050–1056
- Meert JG, Santosh M (2017) The Columbia supercontinent revisited. *Gondwana Res* 50:67–83
- Meert JG, Pandit MK, Kamenov GD (2013) Further geochronological and paleomagnetic constraints on Malani (and pre-Malani) magmatism in NW India. *Tectonophysics* 608:1254–1267
- Meert JG, Pandit MK, Pivarunas A, Katusin K, Sinha AK (2017) India and Antarctica in the Precambrian: a brief analysis. *Geol Soc Spec Publ* 457:339–351
- Middlemost EAK (1994) No naming materials in the magma/igneous rock system. *Earth Sci Rev* 37:215–224
- Miller C, Klötzli U, Frank W, Thöni M, Grasemann B (2000) Proterozoic crustal evolution in the NW Himalaya (India) as recorded by circa 1.80 Ga mafic and 1.84 Ga granitic magmatism. *Precambrian Res* 103:191–206
- Montel JM, Vielzeuf D (1997) Partial melting of metagreywackes. Part II compositions of minerals and melts *Contrib to Mineral Petrol* 128:176–196
- Mukherjee PK, Jain AK, Singhal S, Singha NB, Singh S, Kumud K, Seth P, Patel RC (2019) U-Pb zircon ages and Sm-Nd isotopic characteristics of the lesser and great Himalayan sequences, Uttarakhand Himalaya, and their regional tectonic implications. *Gondwana Res* 75:282–297
- Müller D, Rock NMS, Groves DI (1992) Geochemical discrimination between shoshonitic and potassic volcanic rocks in different tectonic settings: a pilot study. *Mineral Petrol* 46:259–289
- Nachit H, Ibhi A, Abia EH, Ben Ohoud M (2005) Discrimination between primary magmatic biotites, reequilibrated biotites and neofomed biotites. *Comptes Rendus Geosci* 337:1415–1420
- Nasipuri P, Saha L, Hangqiang X, et al (2019) Paleoproterozoic Crustal Evolution of the Bundelkhand Craton, North Central India. In: Kranendonk MJ Van, Bennett VC, Hoffmann JE (eds) *Earth’s Oldest Rocks (Second Edition)*, Second Edi. Elsevier, pp 793–817
- Newton RC, Charlu TV, Kleppa OJ (1980) Thermochemistry of the high structural state plagioclases. *Geochim Cosmochim Acta* 44:933–941
- Paces JB, Miller JD (1993) Precise U-Pb ages of Duluth Complex and related mafic intrusions, northeastern Minnesota: Geochronological insights to physical, petrogenetic, paleomagnetic, and tectonomagmatic processes associated with the 1.1 Ga Midcontinent Rift System. *Journal of Geophysical Research: Solid Earth* 98(B8):13997–14013
- Pandit MK, Khatatneh MK (1998) Geochemical constraints on anorogenic felsic plutonism in North Delhi Fold Belt, Western India. *Gondwana Res* 1:247–255
- Pant NC, Kundu A, Kumar R et al (2006) Palaeoproterozoic metamorphism in the Jeori-Wangtu gneissic complex (JWGC), western Himalayas. *J Asian Earth Sci* 26:545–604
- Pathak M, Kumar S (2019) Petrology, geochemistry and zircon U–Pb–Lu–Hf isotopes of paleoproterozoic granite gneiss from Bomdila in the western arunachal himalaya, ne India. *Geol Soc Spec Publ* 481:341–377
- Patiño Douce AE, Harris N (1998) Experimental constraints on Himalayan anatexis. *J Petrol* 39:689–710
- Patiño Douce AE, Johnston AD (1991) Phase equilibria and melt productivity in the pelitic system: implications for the origin of peraluminous granitoids and aluminous granulites. *Contrib Mineral Petrol* 107:202–218
- Payne JL, Hand M, Barovich KM, Reid A, Evans DAD (2009) Correlations and reconstruction models for the 2500–1500 ma evolution of the Mawson continent. *Geol Soc London Spec Publ* 323:319–355
- Pearce JA, Harris NBW, Tindle A (1984) Trace element discrimination diagrams for the tectonic interpretation of granitic rocks. *J Petrol* 25:956–983
- Phukon P, Sen K, Srivastava HB, Singhal S, Sen A (2018) U-Pb geochronology and geochemistry from the Kumaun Himalaya, NW India, reveal Paleoproterozoic arc magmatism related to formation of the Columbia supercontinent. *Bull Geol Soc Am* 130:1164–1176

- Pickering J, Johnston AD (1998) Fluid-absent melting behavior of a two-Mica Metapelite: experimental constraints on the origin of Black Hills granite. *J Petrol* 39:1787–1804
- Pradhan V, Meert J, Pandit M et al (2012) Tectonic evolution of the Precambrian Bundelkhand craton, Central India: insights from paleomagnetic and geochronological studies on the mafic dyke swarms. *Precambrian Res* 198–199:51–76
- Prakash A, Piazo S, Saha L, Bhattacharya A, Pal DK, Sarkar S (2018) Deformation behavior of migmatites: insights from microstructural analysis of a garnet–sillimanite–mullite–quartz–feldspar-bearing anatectic migmatite at Rampura–Agucha, Aravalli–Delhi Fold Belt, NW India. *Int J Earth Sci* 107:2265–2292
- Rao DR, Sharma KK, Choubey VM (1991) Megacrysts in the granitoid rocks of Wangtu gneissic complex, Satluj valley, Kinnuar District, Himachal Pradesh. *Jour Him Geol* 2:39–46
- Rao DR, Sharma KK, Gopalan K (1995) Granitoid rocks of Wangtu gneissic complex, Himachal Pradesh: an example of in situ fractional crystallisation and volatile action. *J Geol Soc Ind* 46:5–14
- Richards A, Argles T, Harris N et al (2005) Himalayan architecture constrained by isotopic tracers from clastic sediments. *Earth Planet Sci Lett* 236:773–796
- Richards A, Parrish R, Harris NBW, Argles T, Zhang L (2006) Correlation of lithotectonic units across the eastern Himalaya, Bhutan. *Geology* 34:341–344
- Rogers JJW (2009) A history of continents in the past three billion years. *J Geol* 104:91–107
- Rogers JJW, Santosh M (2002) Configuration of Columbia, a Mesoproterozoic supercontinent. *Gondwana Res* 5:5–22
- Rogers JJW, Santosh M (2005) *Continents and supercontinents*. Oxford University Press 7:653
- Saha D (2013) Lesser Himalayan sequences in eastern Himalaya and their deformation: implications for Paleoproterozoic tectonic activity along the northern margin of India. *Geosci Front* 4:289–304
- Saha L, Bhowmik SK, Fukuoka M, Dasgupta S (2008) Contrasting episodes of regional granulite-facies metamorphism in enclaves and host gneisses from the Aravalli - Delhi Mobile Belt, NW India. *J Petrol* 49:107–128
- Saha L, Frei D, Gerdes A, Pati JK, Sarkar S, Patole V, Bhandari A, Nasipuri P (2016) Crustal geodynamics from the Archaean Bundelkhand Craton, India: constraints from zircon U–Pb–Hf isotope studies. *Geological Magazine* 153(1):179–192
- Sanyal S, Sengupta P (2012) Metamorphic evolution of the Chotanagpur granite gneiss complex of the east Indian shield: current status. *Geol Soc London Spec Publ* 365:117–145
- Satyanarayanan M, Balaram V, Sawan SS et al (2018) Rapid determination of REEs, PGEs, and other trace elements in geological and environmental materials by high resolution inductively coupled plasma mass spectrometry. *At Spectrosc* 39:1–15
- Sen K, Tripathi K, Dubey AK (2013) Is the north Indian continental margin a Palaeo-Proterozoic magmatic arc? Insights from magnetomineralogy and geochemistry of the Wangtu gneissic complex, Himachal lesser Himalaya. *Curr Sci* 104:1–8
- Sen A, Sen K, Srivastava HB, Singhal S, Phukon P (2019) Age and geochemistry of the paleoproterozoic bhatwari gneiss of garhwal lesser himalaya, nw India: implications for the pre-himalayan magmatic history of the lesser himalayan basement rocks. *Geol Soc Spec Publ* 481:319–339
- Singh S (1993) Deformation and strain pattern in parts of the Jutogh Nappe along the Sutlej valley in Jeori-Wangtu region, Himachal Pradesh, India. *J Himal Geol* 4:41–55
- Singh S (2020) Himalayan Magmatism through space and time. *Episodes* 43:358–368
- Singh S, Jain AK (2003) Himalayan granitoids. *J Virtual Explor* 11:1–20
- Singh S, Mukherjee PK, Jain AK et al (2003) Source characterization and possible emplacement mechanism of collision-related Gangotri Leucogranite along Bhagirathi Valley, NW-Himalaya. *J Virtual Explor* 11:60–73
- Singh S, Jain AK, Barley ME (2009) SHRIMP U–Pb c. 1860 Ma anorogenic magmatic signatures from the NW Himalaya: implications for palaeoproterozoic assembly of the Columbia supercontinent. *Geol Soc Spec Publ* 323:283–300
- Söderlund U, Bleeker W, Demirev K, Srivastava RK, Hamilton M, Nilsson M, Pesonen LJ, Samal AK, Jayananda M, Ernst RE, Srinivas M (2019) Emplacement ages of Paleoproterozoic mafic dyke swarms in eastern Dharwar craton, India: implications for paleoreconstructions and support for a ~30° change in dyke trends from south to north. *Precambrian Res* 329:26–43
- Stein HJ, Hannah JL, Zimmerman A, Markey RJ, Sarkar SC, Pal AB (2004) A 2.5 Ga porphyry Cu–Mo–Au deposit at Malanjkhanda, central India: implications for Late Archaean continental assembly. *Precambrian Research* 134(3–4):189–226
- St-Onge MR, Wodicka N, Ijewliw O (2007) Polymetamorphic evolution of the trans-Hudson orogen, Baffin Island, Canada: integration of petrological, structural and geochronological data. *J Petrol* 48:271–302
- Tajčmanová L, Konopásek J, Connolly JAD (2007) Diffusion-controlled development of silica-undersaturated domains in felsic granulites of the bohemian massif (Variscan belt of Central Europe). *Contrib Mineral Petrol* 153:237–250
- Tinkham DK, Zuluaga CA, Stowell HH (2001) Metapelite phase equilibria modeling in MnNCKFMASH: the effect of variable Al₂O₃ and MgO/(MgO+FeO) on mineral stability. *Geol Mater Res* 3:1–42
- Tinkham DK, Zuluaga CA, Stowell HH (2003) Metapelite phase equilibria modeling in MnNCKFMASH: the effect of variable Al₂O₃ and MgO/(MgO+FeO) on mineral stability. *Am Mineral* 88:1174
- Tripathi K, Sen K, Dubey AK (2012) Modification of fabric in pre-Himalayan granitic rocks by post-emplacement ductile deformation: insights from microstructures, AMS, and U–Pb geochronology of the Paleozoic Kinnaur Kailash granite and associated Cenozoic leucogranites of the south Tibetan. *Int J Earth Sci* 101:761–772
- Upreti BN (1999) An overview of the stratigraphy and tectonics of the Nepal Himalaya. *J Asian Earth Sci* 17:571–606
- Valdiya KS (2016) *The making of India*. Springer
- Van Kranendonk MJ, Collins WJ (1998) Timing and tectonic significance of late Archaean, sinistral strike-slip deformation in the central Pilbara structural corridor, Pilbara Craton, Western Australia. *Precambrian Res* 88:207–232
- Vielzeuf D, Holloway JR (1988) Experimental determination of the fluid-absent melting relations in the pelitic system. *Contrib Mineral Petrol* 98:257–276
- Vielzeuf D, Montel JM (1994) Partial melting of metagreywackes. Part I. fluid-absent experiments and phase relationships. *Contrib Mineral Petrol* 117:375–393
- Vigneresse JL, Barbey P, Cuney M (1996) Rheological transitions during partial melting and crystallization with application to felsic magma segregation and transfer. *J Petrol* 37:1579–1600
- White RW, Powell R, Holland TJB, Worley BA (2000) The effect of TiO₂ and Fe₂O₃ on metapelitic assemblages at greenschist and amphibolite facies conditions: mineral equilibria calculations in the system K₂O–FeO–MgO–Al₂O₃–SiO₂–H₂O–TiO₂–Fe₂O₃. *J Metamorph Geol* 18:497–511
- White RW, Powell R, Holland TJB (2001) Calculation of partial melting equilibria in the system Na₂O–CaO–K₂O–FeO–MgO–Al₂O₃–SiO₂–H₂O (NCKFMASH). *J Metamorph Geol* 19:139–153
- White RW, Powell R, Holland TJB (2007) Progress relating to calculation of partial melting equilibria for metapelites. *J Metamorph Geol* 25:511–527
- White RW, Powell R, Holland TJB, Johnson TE, Green ECR (2014) New mineral activity-composition relations for thermodynamic calculations in metapelitic systems. *J Metamorph Geol* 32:261–286
- Windley B (1985) The Himalayas. *Geol Today* 1:169–173

- Wu C-M, Hongxu C (2014) Revised Ti-in-biotite geothermometer for ilmenite- or rutile-bearing crustal metapelites. *Sci Bull* 60:116–121
- Zhao G, Zhai M (2013) Lithotectonic elements of Precambrian basement in the North China Craton: review and tectonic implications. *Gondwana Res* 23:1207–1240
- Zhao G, Cawood PA, Wilde SA, Sun M (2002) Review of global 2.1–1.8 Ga orogens: implications for a pre-Rodinia supercontinent. *Earth-Science Rev* 59:125–162
- Zhao G, Li S, Sun M, Wilde SA (2011) Assembly, accretion, and breakup of the Palaeo-Mesoproterozoic Columbia supercontinent: record in the North China Craton revisited. *Int Geol Rev* 11–12:1351–1356

Publisher's note Springer Nature remains neutral with regard to jurisdictional claims in published maps and institutional affiliations.